



National Library
of Canada

Bibliothèque nationale
du Canada

Acquisitions and
Bibliographic Services Branch

Direction des acquisitions et
des services bibliographiques

395 Wellington Street
Ottawa, Ontario
K1A 0N4

395, rue Wellington
Ottawa (Ontario)
K1A 0N4

Your file Votre référence

Our file Notre référence

NOTICE

The quality of this microform is heavily dependent upon the quality of the original thesis submitted for microfilming. Every effort has been made to ensure the highest quality of reproduction possible.

If pages are missing, contact the university which granted the degree.

Some pages may have indistinct print especially if the original pages were typed with a poor typewriter ribbon or if the university sent us an inferior photocopy.

Reproduction in full or in part of this microform is governed by the Canadian Copyright Act, R.S.C. 1970, c. C-30, and subsequent amendments.

AVIS

La qualité de cette microforme dépend grandement de la qualité de la thèse soumise au microfilmage. Nous avons tout fait pour assurer une qualité supérieure de reproduction.

S'il manque des pages, veuillez communiquer avec l'université qui a conféré le grade.

La qualité d'impression de certaines pages peut laisser à désirer, surtout si les pages originales ont été dactylographiées à l'aide d'un ruban usé ou si l'université nous a fait parvenir une photocopie de qualité inférieure.

La reproduction, même partielle, de cette microforme est soumise à la Loi canadienne sur le droit d'auteur, SRC 1970, c. C-30, et ses amendements subséquents.

UNIVERSITY OF ALBERTA

**Intergrain Flux Motion and Critical State in
Y - Ba - Cu - O Ceramic Superconductors**

BY



Loran Friedrich

A thesis submitted to the Faculty of Graduate Studies and Research in partial fulfillment of the requirements for the degree of Master of Science.

IN

SOLID STATE PHYSICS

DEPARTMENT OF PHYSICS

EDMONTON, ALBERTA

FALL, 1992



National Library
of Canada

Bibliothèque nationale
du Canada

Canadian Theses Service Service des thèses canadiennes

Ottawa, Canada
K1A 0N4

The author has granted an irrevocable non-exclusive licence allowing the National Library of Canada to reproduce, loan, distribute or sell copies of his/her thesis by any means and in any form or format, making this thesis available to interested persons.

The author retains ownership of the copyright in his/her thesis. Neither the thesis nor substantial extracts from it may be printed or otherwise reproduced without his/her permission.

L'auteur a accordé une licence irrévocable et non exclusive permettant à la Bibliothèque nationale du Canada de reproduire, prêter, distribuer ou vendre des copies de sa thèse de quelque manière et sous quelque forme que ce soit pour mettre des exemplaires de cette thèse à la disposition des personnes intéressées.

L'auteur conserve la propriété du droit d'auteur qui protège sa thèse. Ni la thèse ni des extraits substantiels de celle-ci ne doivent être imprimés ou autrement reproduits sans son autorisation.

ISBN 0-315-77145-3

Canada

UNIVERSITY OF ALBERTA

RELEASE FORM

NAME OF AUTHOR: Loran Friedrich

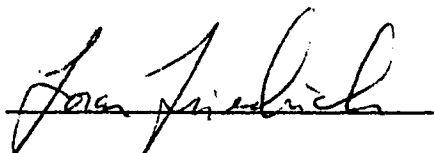
TITLE OF THESIS: Intergrain Flux Motion and Critical State of Y - Ba - Cu - O
Ceramic Superconductors

DEGREE: Master of Science

YEAR THIS DEGREE WAS GRANTED: 1992

Permission is hereby granted to the University of Alberta Library to reproduce single copies of this thesis and to lend or sell such copies for private, scholarly or scientific research purposes only.

The author reserves all other publication and other rights in association with the copyright in the thesis, and except as hereinbefore provided neither the thesis nor any substantial portion thereof may be printed or otherwise reproduced in any material form whatever without the author's prior written permission.

A handwritten signature in cursive script, reading "Loran Friedrich", written over a horizontal line.

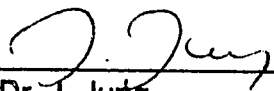
Loran Friedrich
R.R. #2 Morinville
Alberta
Canada
T0G 1P0

August 14, 1992

UNIVERSITY OF ALBERTA

FACULTY OF GRADUATE STUDIES AND RESEARCH

The undersigned certify that they have read, and recommend to the Faculty of Graduate Studies and Research for acceptance, a thesis entitled Intergrain Flux Motion and Critical State of Y - Ba - Cu - O Ceramic Superconductors submitted by Loran Friedrich in partial fulfillment of the requirements for the degree of Master of Science in Solid State Physics.



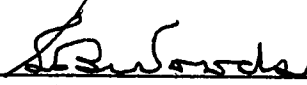
Dr. J. Jung



Dr. J. Tuszynski



Dr. M. A. -K Mohamed



Dr. S. Woods



Dr. R. Fedosejevs

August 14, 1992

ABSTRACT

Intergrain flux motion and the critical state of Y - Ba - Cu - O ceramic superconductors are discussed. The procedure of measuring the dc magnetization with increasing temperature after quickly cooling the sample reveals an increase in magnetization dependent on magnetic field and temperature. The increase in magnetization is the result of the depinning and expulsion of intergrain flux. The decoupling of the grains (decreasing magnetization) is also noted. The measurements are made on pure $\text{YBa}_2\text{Cu}_3\text{O}_{7-x}$, $\text{YBa}_2\text{Cu}_3\text{O}_{7-x}+\text{Ag}$ (2% wt.) and $\text{YBa}_2\text{Cu}_3\text{O}_{7-x}+\text{Ag}$ (4% wt.) samples, thereby showing the effect the added silver has on the intergrain flux. Phase diagrams in the (H, T) plane are drawn for each sample. These diagrams display the pinning strengths and the grain coupling strengths of the samples. Furthermore, a T_c for the grain junctions is inferred from the low field region of a phase diagram. The intergrain flux phase lines are compared to the irreversibility line.

A Bean model is extended to discuss disk - shaped ceramic $\text{YBa}_2\text{Cu}_3\text{O}_{7-x}$ superconductors. Both intergrain and intragrain contributions to the shielding field are considered in computer simulations. Fits are made to experimentally obtained shielding field profiles of pressed powder and ceramic samples. An attempt to simulate the shielding field in increase applied field is made.

TABLE OF CONTENTS

1	INTRODUCTION	1
2	FLUX MOTION IN INHOMOGENEOUS CERAMIC SUPER- CONDUCTORS	7
2.1	Introduction	7
2.2	Flux Pinning	8
2.3	Flux Line Motion	9
a)	Depinning of Flux	9
b)	Flux Lattice Melting	9
c)	Equation of Motion	10
2.4	Experimental Objectives	10
2.5	Experimental Procedures	11
a)	Sample Preparation and Descriptions	11
b)	Magnetization Measurements	12
c)	Resistance Measurements	13
2.6	Experimental Results	14
a)	Zero Field Cooled Experiments	14
b)	Field Cooled Experiments	15
c)	Magnetic Moment Increase Rates	19

d)	Resistance Measurements	21
2.7	Discussion	27
a)	Pinning Effects	27
b)	Field Versus Temperature Phase Diagrams	28
3	EXTENDED CRITICAL STATE MODEL FOR A DISK SHAPED TYPE II SUPERCONDUCTOR	39
3.1	Introduction	39
3.2	Bean Model of Critical-State Superconductors	40
3.3	Granular Superconductors	42
3.4	Type II Superconductors in the Critical-State	44
3.5	Critical-State Model	46
a)	Critical-State Model for a Disk-Shaped Sample	46
b)	Extended Critical-State Model	48
3.6	Critical-State Model Simulation Constraints	49
a)	Intergrain Critical Currents	49
b)	Intragrain Shielding Field Simulation Constraints	51
3.7	Critical-State Model Simulation Results and Discussions	51
a)	Full Critical State Shielding Field Profiles	51
b)	Intergrain Shielding Field Profiles	53
c)	Intragrain Shielding Field Profiles	57
d)	Ceramic Superconductor's Shielding Field Profiles	61

e)	Shielding Fields Dependent on Applied Field	61
4	SUMMARY	70
	BIBLIOGRAPHY	74

LIST OF FIGURES

1.1	<i>a. Hysteretic behavior of a type I superconductor. b. Reversible behavior of a type II superconductor.</i>	5
2.1	<i>The standard four probe experimental setup used for the measurements of resistance in $YBa_2Cu_3O_{7-x}$ (sample RJJ1A).</i>	14
2.2	<i>Zero field cooling and field cooling magnetization measurements made on $YBa_2Cu_3O_{7-x}$ sample in an applied field of 10 G.</i>	16
2.3	<i>Zero field cooling and field cooling magnetization measurements (FC measurements made at increasing temperature) made on $YBa_2Cu_3O_{7-x}$ sample in an applied field of 10 G.</i>	17
2.4	<i>Magnetic moment measurements of pure $YBa_2Cu_3O_{7-x}$ (RNG9) in various applied fields. The applied fields are 15, 20, 30, 50, 70 and 100 G for the solid, dashed, dotted, double dashed, triple dashed, and dot dashed lines.</i>	18
2.5	<i>Magnetic moment measurements of $YBa_2Cu_3O_{7-x} + Ag$ (2% wt.) (RNG6) in various applied fields. The applied fields are 15, 20, 30, 50, 70 and 100 G for the solid, dashed, dotted, double dashed, triple dashed, and dot dashed lines.</i>	19
2.6	<i>Magnetic moment measurements of $YBa_2Cu_3O_{7-x} + Ag$ (4% wt.) (RNG10) in various applied fields. The applied fields are 15, 20, 30, 50, 70 and 100 G for the solid, dashed, dotted, double dashed, triple dashed, and dot dashed lines.</i>	20

2.7	<i>Magnetic moment measurements of $YBa_2Cu_3O_{7-x}$ + Ag (4% wt.) (RNG10) in various applied fields. The applied fields are 15, 20, 30, 50, 70 and 100 G for the solid, dashed, dotted, double dashed, triple dashed, and dot dashed lines.</i>	21
2.8	<i>Magnetic moment as a function of time in the field - cooled $YBa_2Cu_3O_{7-x}$ sample (RJJ1A) at 5 G. The temperature of the measurements is 85.5 and 86.5 K.</i>	22
2.9	<i>Magnetic moment as a function of time in the field - cooled $YBa_2Cu_3O_{7-x}$ sample (RJJ1A) at 5 G. The temperature of the measurements is 87.5 and 88.0 K.</i>	23
2.10	<i>The Meissner moment increase rate measured on the $YBa_2Cu_3O_{7-x}$ sample (RJJ1A) versus temperature in an applied field of 5 G.</i>	24
2.11	<i>The Meissner moment increase rate measured on the $YBa_2Cu_3O_{7-x}$ sample (RJJ1A) versus temperature in an applied field of 100 G.</i>	25
2.12	<i>Magnetic moment vs. temperature measurements of the $YBa_2Cu_3O_{7-x}$ sample in an applied field of 5 G.</i>	26
2.13	<i>FCI measurements (fast cooling) on $YBa_2Cu_3O_{7-x}$ (RNG9) (dotted line), $YBa_2Cu_3O_{7-x}$ + Ag (2% wt.) (RNG6) (solid line) and $YBa_2Cu_3O_{7-x}$ + Ag (4% wt.) (RNG10) (dashed line) in an applied field of 20 G.</i>	27
2.14	<i>FCI measurements on samples $YBa_2Cu_3O_{7-x}$ (RNG9) (dashed line) and RJJ1A (solid line) in an applied field of 40 G.</i>	29
2.15	<i>General phase diagram of applied field versus temperature for ceramic superconducting samples.</i>	30

2.16	<i>Phase diagram of applied field versus onset temperature for samples $YBa_2Cu_3O_{7-x}$ (RNG9) (X's), $YBa_2Cu_3O_{7-x} + Ag$ (2% wt.) (RNG6) (triangles) and $YBa_2Cu_3O_{7-x} + Ag$ (4% wt.) (RNG10) (circles).</i> . . .	32
2.17	<i>Phase diagram of applied field versus depinning completion temperatures for samples $YBa_2Cu_3O_{7-x}$ (RNG9) (X's), $YBa_2Cu_3O_{7-x} + Ag$ (2% wt.) sample (RNG6) (triangles) and $YBa_2Cu_3O_{7-x} + Ag$ (4% wt.) sample (RNG10) (circles).</i>	34
2.18	<i>Phase diagram of applied field versus the onset of depinning and depinning completion temperatures for the pure $YBa_2Cu_3O_{7-x}$ samples RNG9 (X,+) and RJJ1A (squares,circles). The irreversibility line for intragranular depinning measured on the pressed - powder $YBa_2Cu_3O_{7-x}$ sample RJJ1 [32] is given by the triangles. RJJ1 exhibited inter-grain depinning before the pulverizing procedure.</i>	36
2.19	<i>Phase diagram of applied field versus the onset of depinning and depinning completion temperatures for the $YBa_2Cu_3O_{7-x} + 2\% Ag$ (wt.) samples RNG6 (X,+) and RAJJ1 (squares,circles).</i>	37
2.20	<i>Phase diagram of applied field versus onset of depinning and depinning completion temperatures for the pure $YBa_2Cu_3O_{7-x}$ sample RJJ1A.</i> .	38
3.1	<i>Illustration of Bean's model. Local fields and current density for applied fields parallel to the surface of a slab of thickness x. a) applied field is less than H^* and b) applied field is H^* as entire sample is in the critical state.</i>	41
3.2	<i>Cross-section of a superconducting disk. The critical current distribution is considered as a series of concentric current loops.</i>	47

3.3	<i>Dependence of the transport critical current density on an applied field at 77K. Solid line shows fit used in simulation, circles are the experimentally obtained data [35].</i>	50
3.4	<i>Axial (dashed) and radial (solid) shielding fields produced by intergrain currents only. The disk - shaped sample was in a full critical state and the currents were considered magnetic field dependent. The disk radius and thickness are 8 mm and 2.2 mm respectively.</i>	52
3.5	<i>Partial critical state current distribution. Black areas indicate zero current, white areas indicate maximum current. The contours are in steps of 20A. 55.0, 25.6 and 0.0% of the cross - sectional current area is removed.</i>	54
3.6	<i>Shielding fields produced by intergrain currents only. Solid line is the full critical state. dotted and dashed lines are profiles generated from partial critical state scenarios (25.6% and 55.0 % of the cross - sectional current area removed respectively).</i>	55
3.7	<i>Superconducting disk in a partial critical state current distribution. Here the currents near the disk edges are destroyed due to flux motion. Black areas indicate zero current, white areas indicate maximum current. The contours are in steps of 20A. 0.0, 7.0 and 12.6% of the cross - sectional current area is removed.</i>	56
3.8	<i>Shielding field profiles generated from a full critical state (dotted line), and two partial states (solid line: 7% and dashed line: 13% of cross - sectional current area removed) resulting from flux flow dissipation of current (solid and dashed lines).</i>	58

3.9	<i>Intragranular Shielding Fields. The measured data of Mohamed and Jung [35] of a pressed powdered sample in an applied field of 15 G. (black circles) is compared to the calculation of intragranular shielding fields alone. The parameter ι for the solid line is 30.4 Acm^2, dotted line: 22.4 Acm^2, and the dashed line: 38.4 Acm^2.</i>	59
3.10	<i>The measured data of Mohamed and Jung [35] of a $\text{YBa}_2\text{Cu}_3\text{O}_{7-x}$ ceramic sample in an applied field of 100 G. (black circles) is compared to the calculation of intragranular shielding fields alone (solid line). The parameter ι is 2664 Acm^2.</i>	60
3.11	<i>Shielding field profile of ceramic sample. The measured data of Mohamed and Jung [35] of a ceramic $\text{YBa}_2\text{Cu}_3\text{O}_{7-x}$ sample in an applied field of 15 G. (black circles) is compared to the results of calculation made including both intergranular and intragranular diamagnetic shielding fields.</i>	62
3.12	<i>Dependence of the shielding field of ceramic $\text{YBa}_2\text{Cu}_3\text{O}_{7-x}$ on applied field. [35] Open circle: disk center, squares, triangles, inverted triangles and solid circles: points 2, 4, 6, 8 mm from center.</i>	64
3.13	<i>Current distributions used in calculating the shielding field dependence on applied field. The distributions have 0, 2.6 and 5.73% of cross - sectional current area removed.</i>	66
3.14	<i>Current distributions used in calculating the shielding field dependence on applied field. The distributions have 9.1, 12.6 and 16.0% of cross - sectional current area removed.</i>	67
3.15	<i>Current distributions used in calculating the shielding field dependence on applied field. The distributions have 19.6, 23.3 and 30.9% of cross - sectional current area removed.</i>	68

3.16 *Calculated shielding field dependent on current distribution (applied field). Each successive point on each curve was calculated using 0, 2.6, 5.73, 9.1, 12.6, 16.0, 19.6, 23.3, and 30.9% of cross - sectional current area removed. The curves (circles, x's, triangles, inverted triangles, and diamonds represent 0, 2, 4, 6, 8 mm from the disk center.* 69

CHAPTER ONE

INTRODUCTION

The history of superconductivity begins in 1911 when Kamerlingh Onnes [1], upon achieving temperatures low enough to liquefy helium, did resistive measurements on such materials as mercury, lead and tin. What was observed was the complete disappearance of electrical resistance in the materials. The point at which this vanishing of resistance occurs depends on both the temperature and magnitude of an applied field, ergo defining two material dependent parameters: the critical temperature, T_c and the critical field H_c . Above these values a resistance is present. Experiments which unequivocally demonstrate this phenomenon study the persistent currents set up in rings of superconducting material. Once obtained in the rings, the currents will not reveal any observable dissipation. In fact, careful experiments under specific conditions show that there should be no dissipation up to $10^{10^{10}}$ years [2]! These characteristics describe *perfect conductivity*. It was not until 1933 when Meissner and Ochsenfeld [3] discovered that these superconductors in fact also display *perfect diamagnetism*. This means a superconducting sample exposed to an externally applied field expels all magnetic flux from its interior except a thin layer of thickness λ , the magnetic penetration depth, in which the magnetic field decreases exponentially to zero.

Two important theories have emerged and give a satisfactory discussion of the nature of superconductivity. These theories are the BCS theory [4] and the Ginzburg-Landau theory [5]. The BCS theory, named after J. Bardeen, L. N. Cooper, and J. R. Shrieffer, can be described as a pairing theory of superconductivity. The theory states *Cooper Pairs* form as the result of a weak attractive interaction between two electrons. Such an interaction could be an electron - phonon interaction which

aids in forming bound pairs of electrons with equal but opposite momentum and spin. The Cooper pairs, said to be the charge carriers in superconductivity, have a spatial extension of ξ_0 , the Pippard coherence length. The BCS theory also predicts a minimum energy, $E_g = 2\Delta(T)$, needed for the Cooper pairs to be broken and superconductivity quenched. Here, $\Delta(T)$ is a gap parameter and increases from zero at T_c to a limiting value, $\Delta(T \ll T_c) = 3.528kT_c$.

The Ginzburg-Landau (*GL*) theory of superconductivity [5] takes a different approach to explaining the phenomenon. This theory is based on the introduction of a psuedo wave function $\psi = \eta e^{i\phi}$ acting as an order parameter for the superconducting electrons whose density is $n_s = |\psi(x)|^2$. The free energy density of a system where ψ is a slowly varying function in space is written in powers of ψ and $\nabla\psi$, and includes the interaction of a magnetic field. Its form is:

$$f = f_{n0} + \alpha |\psi|^2 + \frac{\beta}{2} |\psi|^4 + \frac{1}{2m^*} \left| \left(\frac{\hbar}{i} \vec{\nabla} - \frac{e^*}{c} \vec{A} \right) \psi \right|^2 + \frac{H^2}{8\pi}. \quad (1.1)$$

Here, f_{n0} is the free energy density in the normal state, \vec{A} is the magnetic vector potential, H is the local magnetic field, e^* is the charge, $e^* = 2e$, and m^* is the mass of the superconducting pairs, $m^* = 2m_e$. Minimization of the free energy by variational techniques allows for the writing of a GL differential equation for ψ similiar to Schrödinger's equation excepting a non-linear term.

$$\alpha\psi + \beta |\psi|^2 \psi + \frac{1}{2m^*} \left(\frac{\hbar}{i} \vec{\nabla} - \frac{e^*}{c} \vec{A} \right)^2 \psi = 0. \quad (1.2)$$

The non-linear term will act as a repulsive potential on ψ , thus favouring the solutions where ψ is spatially spread out. Within the framework of this theory, a supercurrent is calculable.

$$\vec{J} = \frac{e^*}{m^*} |\psi|^2 \left(\hbar \vec{\nabla} \phi - \frac{e^*}{c} \vec{A} \right) = e^* |\psi|^2 \vec{v}_s. \quad (1.3)$$

The last form of the supercurrent has e^* , the charge of the superconducting carriers, $|\psi(x)|^2$, the superconducting carrier density, and v_s , the velocity of the carriers.

The GL theory enables the study of nonlinear effects in fields strong enough to affect the superconducting electron density n_s and, correspondingly, its spatial dependence. A characteristic length is also introduced in the GL approach. This is known as the temperature dependent coherence length, $\xi(T)$, which denotes the distance over which ψ varies without energy increase. The temperature dependence is $\xi(T) \sim (T_c - T)^{-\frac{1}{2}}$ and in the limiting case of a pure superconductor far below T_c , $\xi(T) = \xi_0$, ie. the BCS coherence length is achieved.

From the GL theory of superconductivity comes a valuable parameter κ , which is called the Ginzburg-Landau (GL) parameter. κ is the ratio of the two characteristic lengths, the magnetic penetration depth and the coherence length: $\kappa = \frac{\lambda}{\xi}$. λ is known to vary with temperature in a manner similar to ξ ; $\lambda \sim (T_c - T)^{-\frac{1}{2}}$. κ , therefore, remains basically a constant throughout all temperatures below T_c . The GL parameter will in fact classify every superconducting sample as being one type of superconductor or another. For conventional superconductors such as those studied since Onnes' discovery in 1911, $\kappa \ll 1$. Results from the GL theory for such a κ give a positive surface energy at superconducting - normal domain boundaries. This energy must be overcome to vary ψ from its value in the superconducting state, ψ_∞ , to zero. It was Abrikosov [6] in 1957 who studied the effect on the GL theory for the case when $\kappa \gg 1$. Here, since κ is large, the magnetic penetration depth is also extensive and the coherence length is quite small. In contrast to the above, this scenario gives a negative surface energy allowing for the penetration of magnetic flux into the sample and the possibility of flux lattice. The separating point between positive and negative surface energies is given as $\kappa = \frac{1}{\sqrt{2}}$ and, as named by Abrikosov, introduces the *type II superconductivity* (the previous superconducting behavior designated as *type I superconductivity*). Abrikosov was also instrumental in showing that the penetration of magnetic field into samples is in a regular triangular¹ array of flux vortices each carrying a single *quantum of flux* Φ_0 (the flux quantum is defined as $\Phi_0 = \frac{hc}{2e} =$

¹Due to a numerical error, Abrikosov's calculations predicted a square array.

$2.07 \times 10^{-7} \text{ gauss cm}^2$). The penetration of flux into the superconducting sample forms what is called the *mixed state* (type II) or the *intermediate state* (type I), where superconducting and normal domains exist simultaneously. This mixed state has been experimentally proven by performing different decorating experiments [7]. As a consequence of this unique behavior, there arises additional critical field definitions. The particular applied magnetic field when penetration first starts in the type II superconductors is denoted as the *lower critical field*, H_{c1} . Above this field, the mixed state exists. The field at which superconductivity is quenched is expressed as the *upper critical field*, H_{c2} . In fact, theory gives the expression for the upper critical field as

$$H_{c2} = \sqrt{2}(\kappa H_c), \quad (1.4)$$

H_c being the thermodynamically defined value

$$\frac{H_c^2(T)}{8\pi} = f_n(T) - f_s(T). \quad (1.5)$$

Here, f_n and f_s are the free energies for the normal and superconducting states respectively. This form of H_{c2} (1.4) explicitly shows the distinction between the two types of superconductivity. For type I materials $\kappa < \frac{1}{\sqrt{2}}$ which results in $H_{c2} < H_c$ and the hysteretic behavior shown in Fig 1.1 (a). Type II superconductors are characterized by $\kappa > \frac{1}{\sqrt{2}}$. This κ leads to $H_{c2} > H_c$ and a reversible behavior in an increasing and decreasing applied field. Fig. 1.1 (b) shows the reversibility of type II superconductors.

In 1987, a landmark paper by Bednorz and Müller [8] proclaimed the discovery of a new *high temperature* superconducting material. Previous to their discovery, the highest reported transition temperature was 23.3 K in refined Nb_3Ge thin films. The materials studied by Bednorz and Müller were copper oxide based, in particular barium lanthanum copper oxide, and showed the onset of resistivity decreasing rapidly at 35 K. In preparation of the materials, it was noted that the sintering process formed granular bulk samples; superconducting grains were separated by non-stoichiometric

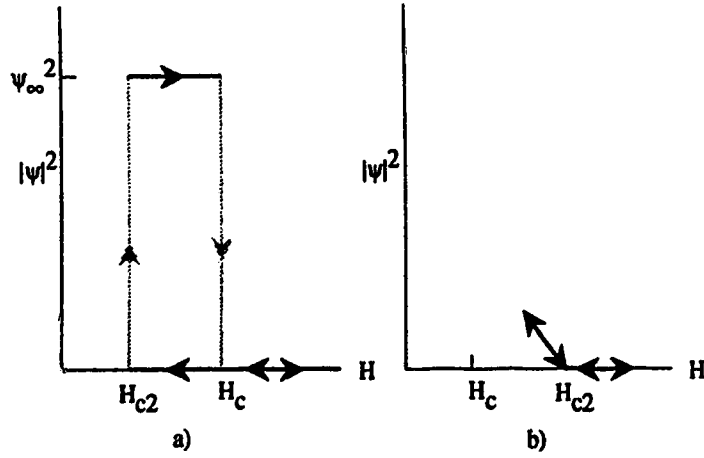


Figure 1.1: *a. Hysteretic behavior of a type I superconductor. b. Reversible behavior of a type II superconductor.*

interface material. While the grains are of a type II superconducting material, the granularity affects the magnetic and electrical properties of bulk samples in a unique manner. The material specific properties such as the magnetic flux behavior, current carrying capabilities and flux - current interaction are of primary importance in understanding the physics of the new superconductors.

To date many magnetic and electrical properties of type II superconductors are still very much a mystery. For instance, flux motion, flux pinning, and flux depinning have been considered from several angles. Work studying these phenomena describes phase lines in the (H, T) plane which determines the state in which the flux lines exist. At a certain applied field and temperature the flux within a superconducting sample can be in one of several states. Samples at low temperatures will have the internal magnetic flux pinned and thus be in a static state. An increase in temperature supplies the necessary thermal energy to depin the trapped flux lines. The temperature at which this occurs is a depinning temperature which depends on the applied magnetic field. Higher temperatures result in increased depinning and subsequent motion of flux lines. Thus the different phases of a type II superconductor in an applied field

can be described.

Much theoretical and experimental work has been done on the flux phase diagram in the (H,T) plane. One approach describes the depinning to be a consequence of the increased thermal energy of each flux line [9, 10, 11]. As the temperature of a sample is increased, the flux lines will achieve an energy capable of depinning them. This energy is called the *flux depinning energy*. Others [12, 13, 14, 15] assert that the flux lines can exist in distinguishable phases (glass, crystalline, solid, fluid). The transition from one phase to another is characterized by the phase lines in the (H,T) plane. Classical elasticity [14, 15] and fluid theories were used to determine and discuss the transitions and phase lines.

This thesis is divided into two parts. The first part (chapter 2) will discuss dc magnetization measurements on $\text{YBa}_2\text{Cu}_3\text{O}_{7-x}$ ceramic samples in low applied magnetic fields. The objectives of those studies was to study the temperature dependence of the intergranular flux depinning process. The methods of measurements utilized, zero field cooling and field cooling measurements, indicate the intergrain magnetic flux is indeed depinned and expelled from the sample. The experimental procedures used in this work allow to determine the temperatures and magnetic fields of the depinning of flux originating from the intergranular pin sites.

In the second part, (chapter 3), the magnetic properties of ceramic $\text{YBa}_2\text{Cu}_3\text{O}_{7-x}$ superconductors are the subject of analysis as an extended *critical-state* model, in particular the *Bean model*, is applied to disk-shaped samples. The results of computer simulations of magnetic shielding field profiles are compared to experimentally obtained profiles. It is shown that those computer computations require consideration of both the intergrain and intragrain shielding currents as well as their modifications due to demagnetization effects at the sample edges.

CHAPTER TWO

FLUX MOTION IN INHOMOGENEOUS CERAMIC SUPERCONDUCTORS

2.1 Introduction

The physical properties of the magnetic flux which has penetrated type II samples is as yet not fully understood. Most theories describing flux motion under different conditions stem from the fundamental ideas proposed by Abrikosov in 1957 [6]. This work gives a very lucrative picture of the flux behavior in bulk type II superconductors by considering the concept of flux vortices. In each vortex there exists one quantum of flux and, circulating it, the necessary shielding supercurrent. The coherence length, ξ , is defined as the distance where the superconducting order parameter, ψ , rises from zero to its value in the superconducting state, ψ_∞ . For each isolated flux, the radius of the current vortex is of length λ , the magnetic penetration depth. In the high temperature superconductors studied, the short coherence length (~ 1.5 nm), large magnetic penetration depth (~ 150 nm) and the extreme directional dependence (anisotropy) of both add to the uniqueness of these materials.

The evolution of the magnetic properties of the type II superconductor in an increasing applied field can be conceptualized in the following way. In very low fields, $H_a < H_{c1}$ the Meissner effect is the predominant characteristic. Here, flux will not penetrate since the self-energy of the flux vortex is greater than the reduction in field energy occurring if penetration had happened. Abrikosov predicted a mixed state would prevail when the applied magnetic field rises above a certain value H_{c1} . At this field the flux vortices will penetrate and subdivide the sample into superconducting and normal domains. It is in this state that the free energy would be lowest. The flux vortices while comprising a mixed state can interact with each other. Accordingly

the vortex density will be determined by these interaction forces and the externally applied field. An increase in field strength will cause the vortex density and vortex - vortex interaction to increase. As the field is eventually increased to the limit where the vortex cores are compressed to the point of overlap, the superconducting order parameter will be reduced to zero and areas of superconductivity will disappear. This applied field is called the upper critical field, H_{c2} .

Thus Abrikosov predicted the basic magnetic behavior of type II superconductors. However, extrapolations to the theory to include the forces affecting individual and collective flux behavior are necessary to aid in describing other flux-related phenomena. A prime example is the pinning of flux lines, its origins and consequences.

2.2 Flux Pinning

Consider a type II superconductor in the mixed state such that the force on individual vortices may be regarded. If a transport current density, \vec{J} , exists within a sample there will exist a Lorentz force acting on the flux vortices. The Lorentz force will cause a flux line to move transversely to the current, thereby creating an electric field antiparallel to \vec{J} . This acts as a resistive voltage causing a dissipation in energy. The superconductor is not able to maintain a persistent current unless there are some *pinning* forces restricting the motion of flux. The pinning forces must be strong enough to overcome the Lorentz forces to keep the flux lines stationary. Pinning is the result of spatial inhomogeneity which affects the characteristic lengths, ξ , λ and the local H_c . The inhomogeneities in the case of type II superconducting ceramics are grain boundaries, voids, impurities, and oxygen content modulation. Effective inhomogeneities must be of the order of λ or ξ and not on the atomic scale where electron scattering is more likely to occur.

2.3 Flux Line Motion

a) Depinning of Flux

Flux lines pinned within a superconducting sample may be depinned and forced to move. In order for a flux line to be depinned, it must first gain enough energy to overcome the pinning forces. This energy is the thermal energy of the line. With sufficient energy, the flux line will be able to escape the pinning potential of the pin site and move under the other present forces (Lorentz).

Flux motion may be thermally activated in a process called *flux creep*. Flux lines jump from one pin site to another without continual motion. Thus thermal fluctuations cause dissipation of superconducting current. However, if the pinning energy is much larger than the thermal energy, the damping of the superconducting current is significantly small (logarithmic time dependence) and thus not a consideration. If the pinning energy is much smaller than the thermal energy, flux flow occurs.

b) Flux Lattice Melting

Flux line motion in superconducting samples may be considered from the point of view of the *flux lattice melting*. The regular array of vortices form a flux lattice characterized by the classical parameters associated with a lattice, such as lattice spacing, lattice point interaction, and elastic constants. It is expected that in the space between the pinning sites, the vortex lattice will be distorted. The forces acting in this deformation are described in the framework of the theory of elasticity [23]. The effective force on the flux lattice depends on the density of the pinning centers, i.e. a high density will cause stronger deformation in the flux line lattice. Work has been done [14, 16, 17, 18] where the flux line lattice displacement due to local forces and thermal fluctuations was discussed. As used in the study of metals,

melting occurs once the lattice points vibrate a certain fraction of their equilibrium separation distance. This is the *Lindeman criterion*. In the case of the flux lattice, melting will allow the flux to flow. Other studies of how the Lindeman criterion is reached and melting occurs are focussed on the order parameter and its thermal fluctuations [19, 20]. Further work considers treating the fluxons as bosons such that the displacements involves a Bose distribution [21].

c) Equation of Motion

To discuss the motion of a flux line within a superconducting material, all the forces acting on it must be considered. The sum of all these forces should equal to zero thereby determining an equation of motion. Such forces are the pinning force, Lorentz force, elastic deformation forces, and the force due to the viscosity of a moving flux line.

2.4 Experimental Objectives

Bulk samples of high temperature superconducting materials have shown a reversibility in their magnetization during the warming and cooling measurements in an applied magnetic field [25]. The irreversibility temperature, T_r , and field, H_r , form the low-temperature and field boundary at which the reversibility range occurs. Müller et al. [22] proposed the existence of different superconducting phases separated by the irreversibility line in the (H, T) plane. Subsequent work analyzed this relationship between T_r and H_r and described it in terms of flux creep [10] and flux pinning models [11]. According to those models, T_r and H_r represent temperatures and fields at which Abrikosov flux depinning occurs. Experimentally resistive superconducting transitions [26, 27], I-V curves, dc and ac magnetization experiments [12] were done in attempts to study this irreversibility line.

It is important to note that much of the above work is based on single crystal or thin film samples. These experiments and others performed on ceramics did not provide adequate information regarding the flux behavior in the intergranular junctions so little was known about the magnetic flux pinned along grain boundaries in ceramics.

Depinning of flux from intergranular junctions is known to occur. This is evident from the measurements of Jung [28] and Mumtaz et al.[29] on both the sintered ceramics and its powdered counterpart. As determined by ac. susceptibility measurements [30], pressed powdered samples have no intergrain junctions. Jung [28] has shown that a powdered sample does not reveal the loss in magnetization recorded in ceramic samples, thereby indicating that the flux depinning is a phenomenon dependent on the intergranular coupling of each sample.

The intergranular junctions can be modified in $\text{YBa}_2\text{Cu}_3\text{O}_{7-x}$ ceramics with the addition of silver. To gain information of the behavior of the intergranular pinned flux, a series of field cooling experiments on various $\text{YBa}_2\text{Cu}_3\text{O}_{7-x} + x\% \text{ Ag wt.}$ ($x = 0, 2, 4$) ceramic samples was performed. It was revealed that the intergrain flux pinning capabilities and characteristics depend heavily on the junctions' properties. The time dependent change of a sample's magnetization was also considered. The results indicated a temperature range in which intergranular flux depinning and motion is most prominent. Comparison with the irreversibility line shows a marked difference in properties of the intergranular and intragranular depinning.

2.5 Experimental Procedures

a) Sample Preparation and Descriptions

Five samples have been used in this study.

- Pure $\text{YBa}_2\text{Cu}_3\text{O}_{7-x}$
 - Sample RJJ1A
 - Sample RNG9
- $\text{YBa}_2\text{Cu}_3\text{O}_{7-x} + 2\% \text{ Ag wt.}$
 - Sample RAJJ1
 - Sample RNG6
- $\text{YBa}_2\text{Cu}_3\text{O}_{7-x} + 4\% \text{ Ag wt.}$
 - Sample RNG10

The samples were prepared by solid state reaction method from metal oxides Y_2O_3 , CuO , and BaCO_3 . After calcining in pure oxygen at 925 C for 2 hours the products were ground, pressed into a pellet and sintered in flowing oxygen at 925 C for 7 hours. Silver was added to $\text{YBa}_2\text{Cu}_3\text{O}_{7-x}$ before the sintering process. Rod-shaped samples of diameter 4.4-4.5 mm and 3.5-3.8 mm thick were then cut from the pellets. One sample (RJJ1A) was sintered as a rod - shaped pellet of diameter 4.5 mm and length of 10.7 mm.

b) Magnetization Measurements

The samples were measured in various applied magnetic fields in an increasing or decreasing temperature. Using a quantum design SQUID magnetometer, the longitudinal component of the magnetization was measured. Zero field cooled (ZFC) and field cooled (FC) measurements were done.

The process of ZFC measurements begins with the sample in no applied magnetic field. The temperature is lowered from above T_c to a specified one well below

T_c . At this point, a field is applied and the sample magnetization is measured as a function of increasing temperature.

There were two procedures followed in making field cooled measurements on the samples. In the FC cases, a magnetic field is applied at a temperature above T_c . In the *FCD* procedure the magnetization measurements are made as a function of decreasing temperature. The other procedure, *FCI*, entails cooling the sample *quickly* through T_c to a temperature, T_{st} well below T_c (down to 10 K). The magnetization measurements are thus made on increasing temperature. To determine the effect the rapid cooling has on the samples, the *FCI* procedure was also carried out for various final temperatures, T_{st} .

The magnetization experiments described above were performed in various applied magnetic fields and temperatures. The applied fields ranged in magnitude from 0.5 G to 1800 G along the cylindrical axis of each sample. Temperatures were varied from 10 K to 100 K. The increments made in increasing and decreasing temperatures were commonly 1.0 K. However, they were often made smaller, 0.5 K, when accurate measurements were desired and up to 5 K when no change in magnetization was expected (usually from 10 to 30 K).

The magnetization relaxation rates (change in magnetic moment with time) were measured as a function of temperature in several applied magnetic fields. The sample was then quickly cooled to 10 K in an applied field. The temperature was then raised to a specific value at which point the magnetization data were measured in time over a period of $10^4 - 10^5$ seconds.

c) *Resistance Measurements*

A standard four probe resistance measurement was made on pure $\text{YBa}_2\text{Cu}_3\text{O}_{7-x}$ sample (RJJ1A) in an attempt to find a resistance due to the flux flowing in the sample.

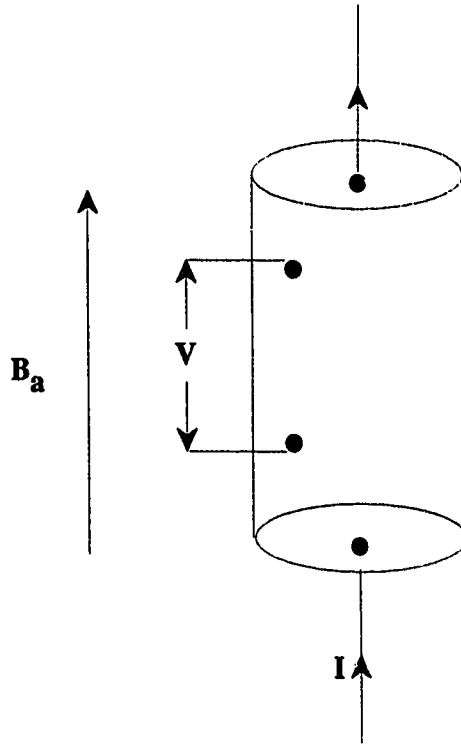


Figure 2.1: *The standard four probe experimental setup used for the measurements of resistance in $YBa_2Cu_3O_{7-x}$ (sample RJJ1A).*

The sample was quickly cooled to 10 K in an applied field of 100 G. A temperature of 72 K was obtained and an applied current of 10 mA was then established. Resistive measurements were taken as a function of temperature. The four probe *Cu* wires were attached to the sample using indium. The configuration used in this experiment is shown in Fig. 2.1.

2.6 Experimental Results

a) Zero Field Cooled Experiments

Zero field cooling experiments were completed using several samples. The data taken on $YBa_2Cu_3O_{7-x}$, presented in Fig 2.2, curve ZFC, display a significant diamagnetic

shielding. With an increase in temperature, the magnetization rapidly increases from negative values to zero at $T = T_c$. The sharpness of the transition reflects the quality of the sample.

b) Field Cooled Experiments

Measurements on Decreasing Temperatures (FCD)

This is the slow cooling procedure most commonly used for FC measurements. The initial temperature of the sample is above T_c ; the starting temperature for the experiments reported here was always being 100 K. Upon cooling the sample at the same applied field as for ZFC, the magnetization measurements were made at regular temperature intervals (Fig. 2.2 curve FCD). The magnetization has a much lower magnitude indicating this procedure allows a significant amount of flux to be trapped in the sample. The difference between the ZFC and FCD curves at low temperatures indicates the the amount of flux trapped during the FCD procedure.

Measurements on Increasing Temperatures (FCI)

In this procedure the sample is *quickly* cooled in an applied field from 100 down to 10 K and measurements are made with increasing temperatures. The data are presented in figure 2.3 as the FCI curve. At low temperatures more trapped flux is observed than there had been in the earlier FC experiment (slow cooling, FCD). As will be shown, this extra flux trapping results from the nonequilibrium conditions due to fast cooling close to T_c .

The sample's magnetization, measured as a function of increasing temperature, remains constant until a temperature, T_o , is achieved. This temperature will be referred to as the *onset temperature* above which magnetic flux is expelled from

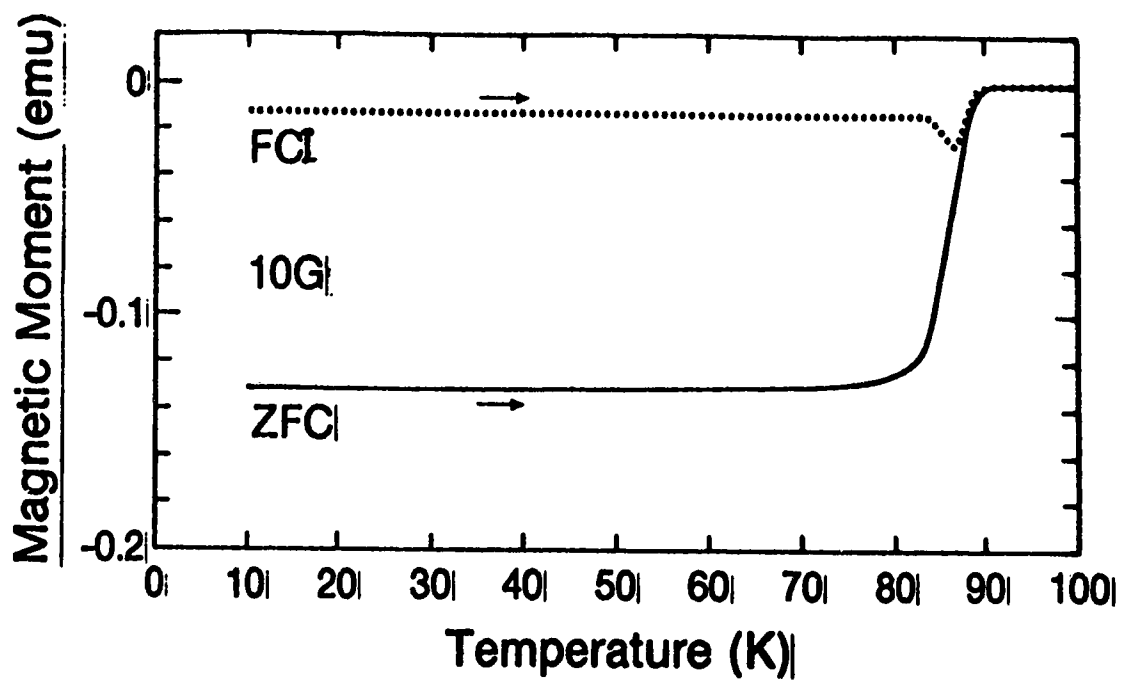


Figure 2.2: Zero field cooling and field cooling magnetization measurements made on $YBa_2Cu_3O_{7-x}$ sample in an applied field of 10 G.

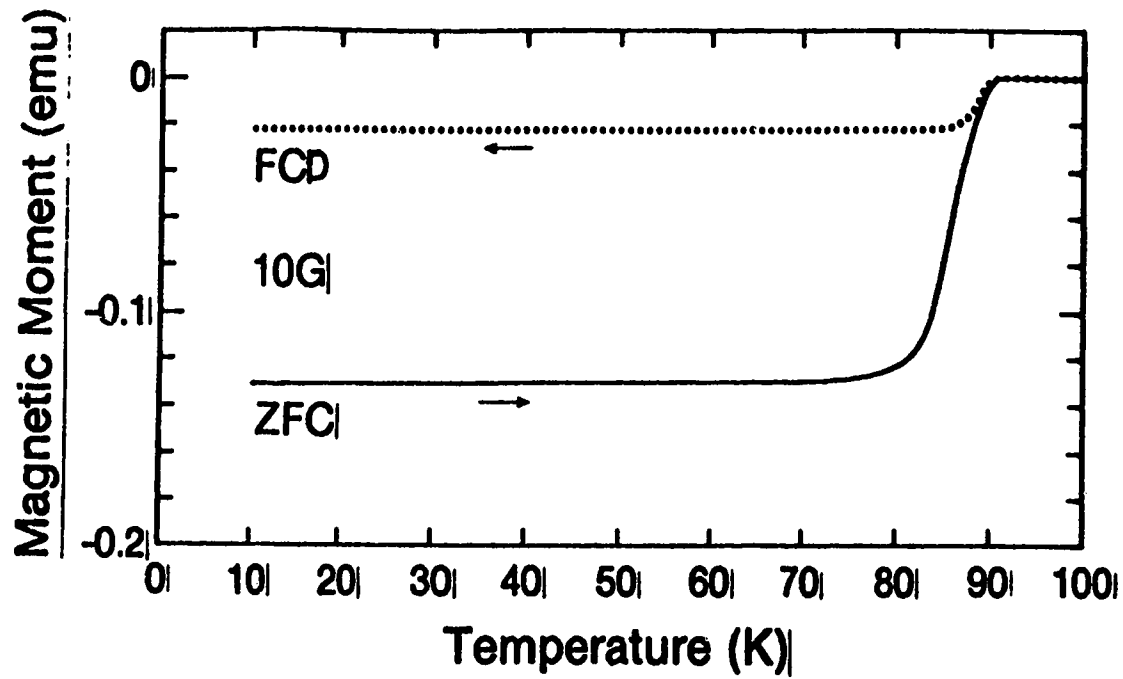


Figure 2.3: Zero field cooling and field cooling magnetization measurements (FC measurements made at increasing temperature) made on $YBa_2Cu_3O_{7-x}$ sample in an applied field of 10 G.

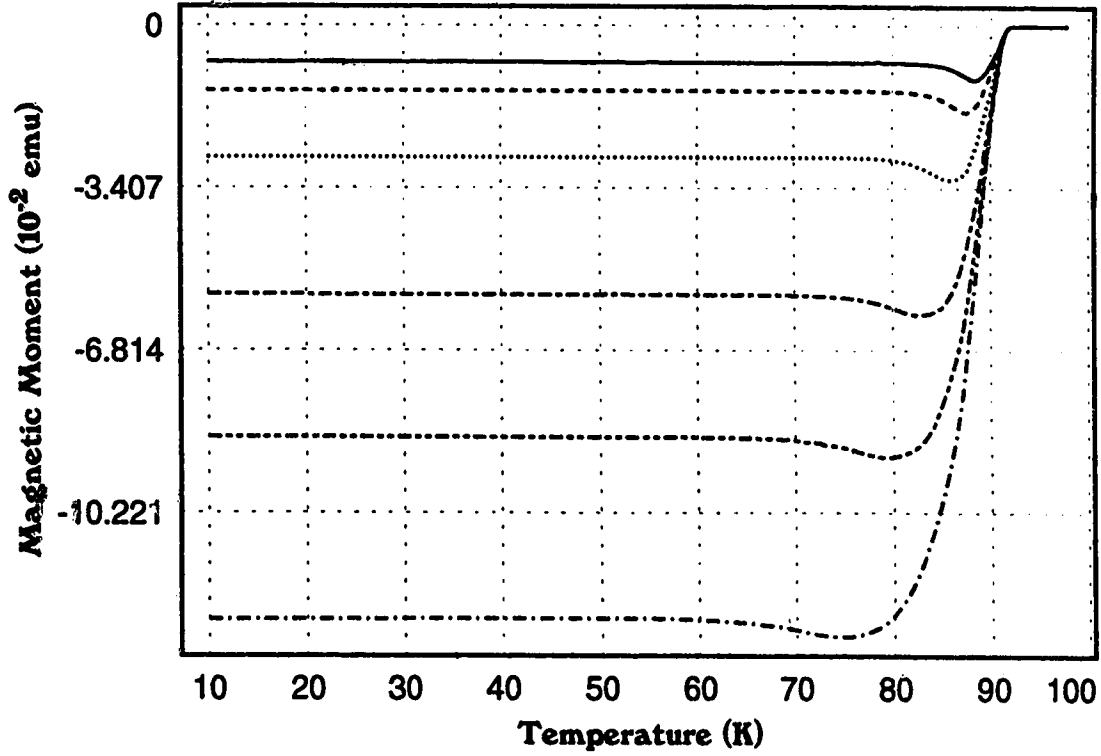


Figure 2.4: *Magnetic moment measurements of pure $YBa_2Cu_3O_{7-x}$ (RNG9) in various applied fields. The applied fields are 15, 20, 30, 50, 70 and 100 G for the solid, dashed, dotted, double dashed, triple dashed, and dot dashed lines.*

the sample. This process continues until a temperature, the *completion temperature* denoted as T_d , is reached. At this point, the magnetization begins once again to decrease as flux moves into the sample. Figs. 2.4, 2.5 and 2.6 show the magnetic moment measurements of the pure $YBa_2Cu_3O_{7-x}$, $YBa_2Cu_3O_{7-x} + Ag$ (2% wt.) and $YBa_2Cu_3O_{7-x} + Ag$ (4% wt.) samples in applied fields up to 100 G.

By changing the temperature, T_{st} , to which the $YBa_2Cu_3O_{7-x}$ sample was quickly cooled, the effect it has on the trapped flux was investigated. The results collected from quickly cooling the sample to temperatures 10, 41, 64, 72 and 82 K in an applied field of 5 G (Fig. 2.7), show no significant changes to the onset or completion temperatures from the data obtained when the sample was cooled to 10

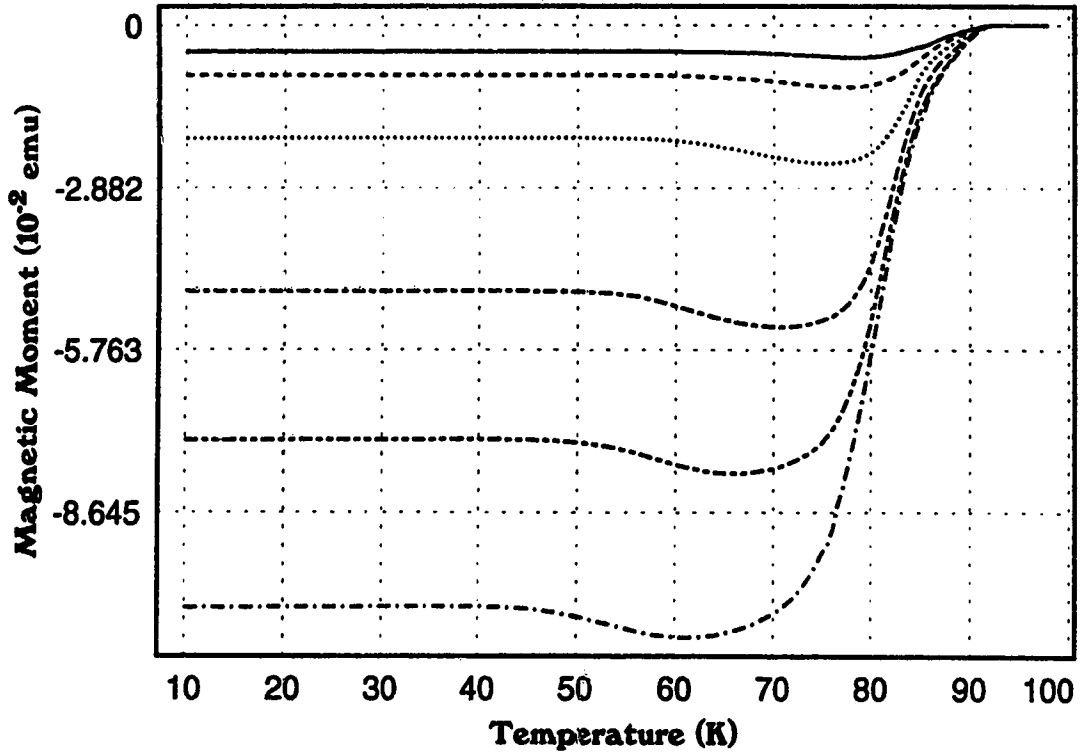


Figure 2.5: *Magnetic moment measurements of $YBa_2Cu_3O_{7-x} + Ag$ (2% wt.) (RNG6) in various applied fields. The applied fields are 15, 20, 30, 50, 70 and 100 G for the solid, dashed, dotted, double dashed, triple dashed, and dot dashed lines.*

K. As long as the temperature range (87 to 84 K), in which depinning occurs, is quickly passed, the temperature to which the sample is cooled does not significantly affect the depinning results.

c) *Magnetic Moment Increase Rates*

The flow of flux out of the samples is evident from the data acquired by measuring the magnetization as a function of time at constant temperature ($T = 85.5$ and 86.5 K Fig. 2.8, $T = 87.5$ and 88.0 K Fig. 2.9). The $YBa_2Cu_3O_{7-x}$ sample (RJJ1A) had been studied this way in two magnetic fields, $H_a = 5$ and 100 G, and the initial logarithmic rates of changing magnetization are given as a function of temperature

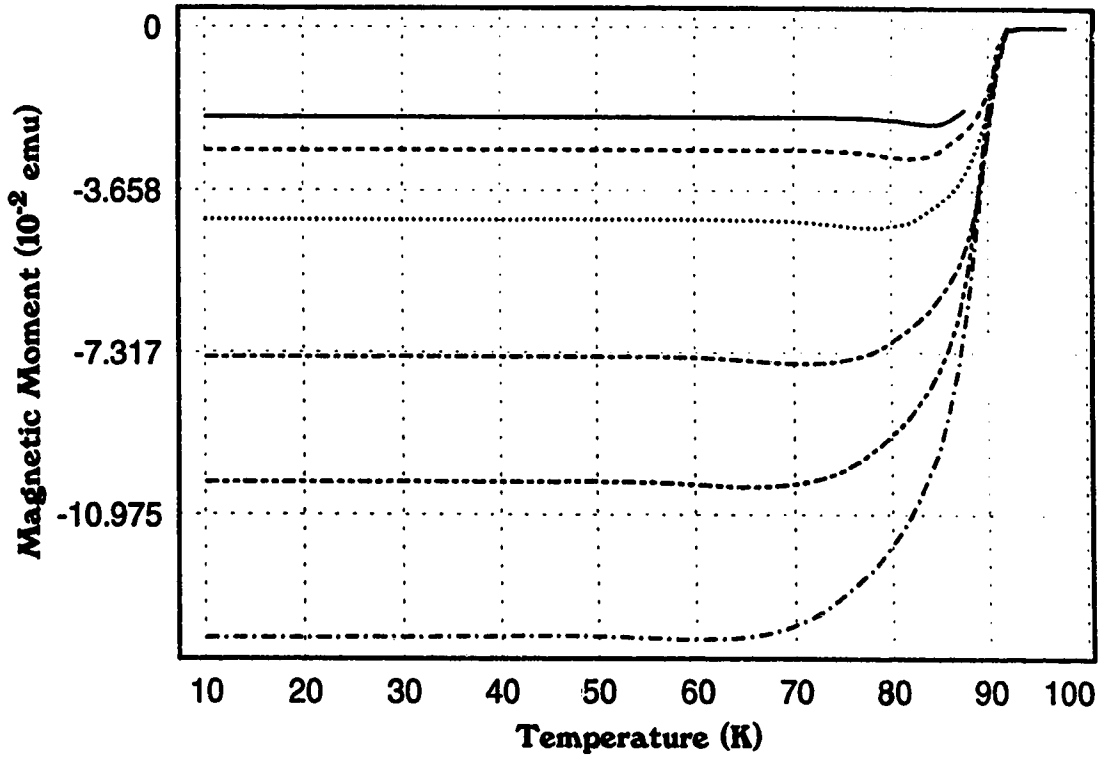


Figure 2.6: *Magnetic moment measurements of $YBa_2Cu_3O_{7-x} + Ag$ (4% wt.) (RNG10) in various applied fields. The applied fields are 15, 20, 30, 50, 70 and 100 G for the solid, dashed, dotted, double dashed, triple dashed, and dot dashed lines.*

($H_a = 5$ G Fig. 2.10 and $H_a = 100$ G Fig. 2.11). The initial rate of changing magnetization was determined by taking a time interval and finding the slope of the data curves as in Figs. 2.8 and 2.9. The time intervals used in calculating the change in magnetization for these four curves was within the range of 100 to 300 seconds.

Note the temperature range in which the decay rates are of significance is shown here as from 85 to 88 K for the applied field of 5 G. At temperatures outside of this range, the change of the magnetic moment of the sample is negligible. Comparison of this range to the FCI data (Fig. 2.12) of the same sample in the same applied field shows the temperature of maximum decay comes at a temperature close to that of maximum magnetization, T_d .

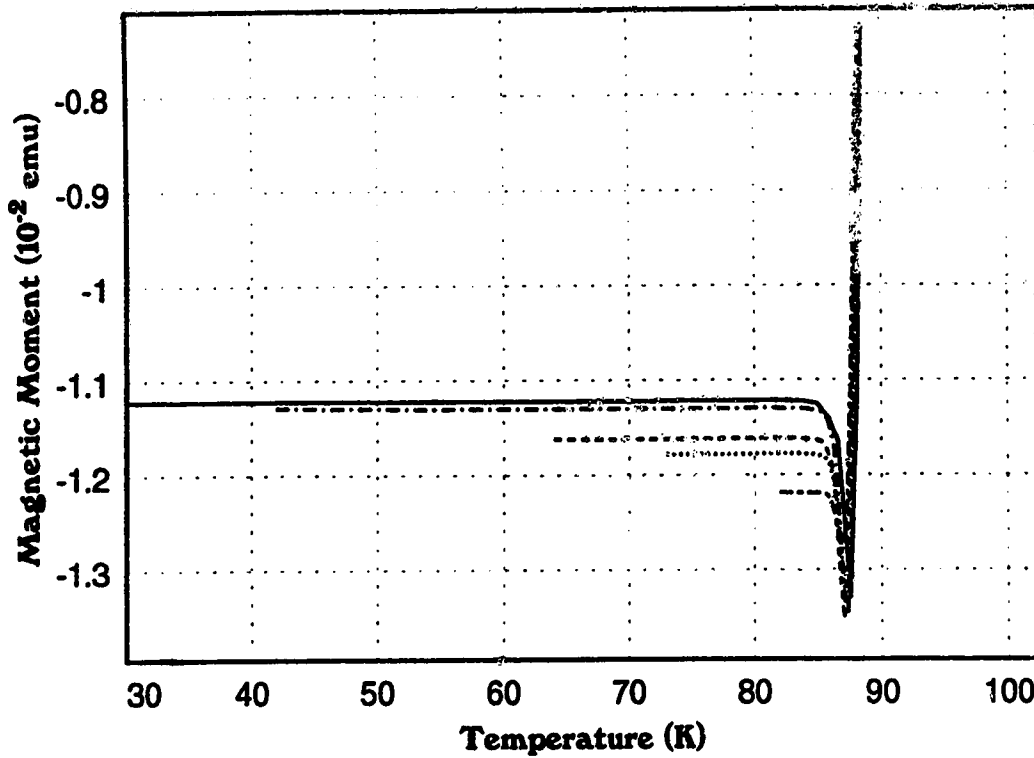


Figure 2.7: *Magnetic moment measurements of $\text{YBa}_2\text{Cu}_3\text{O}_{7-x} + \text{Ag}$ (4% wt.) (RNG10) in various applied fields. The applied fields are 15, 20, 30, 50, 70 and 100 G for the solid, dashed, dotted, double dashed, triple dashed, and dot dashed lines.*

d) Resistance Measurements

The motion of flux within a sample is known to cause dissipation of supercurrent. In an attempt to measure resistance due to the flux motion, the standard four probe technique was employed. The $\text{YBa}_2\text{Cu}_3\text{O}_{7-x}$ sample (RJJ1A) had been cooled quickly in an applied field of 100 G. The temperature was then raised to 72 K, the temperature at which maximum change in magnetization and thusly flux flow is anticipated. The measurements were done using various currents (ranging from 0.1 mA to 20 mA) and voltage readings above 50 nV were taken as the indication of resistance. The results did not reveal any measurable resistance within the sensitivity of the equipment at

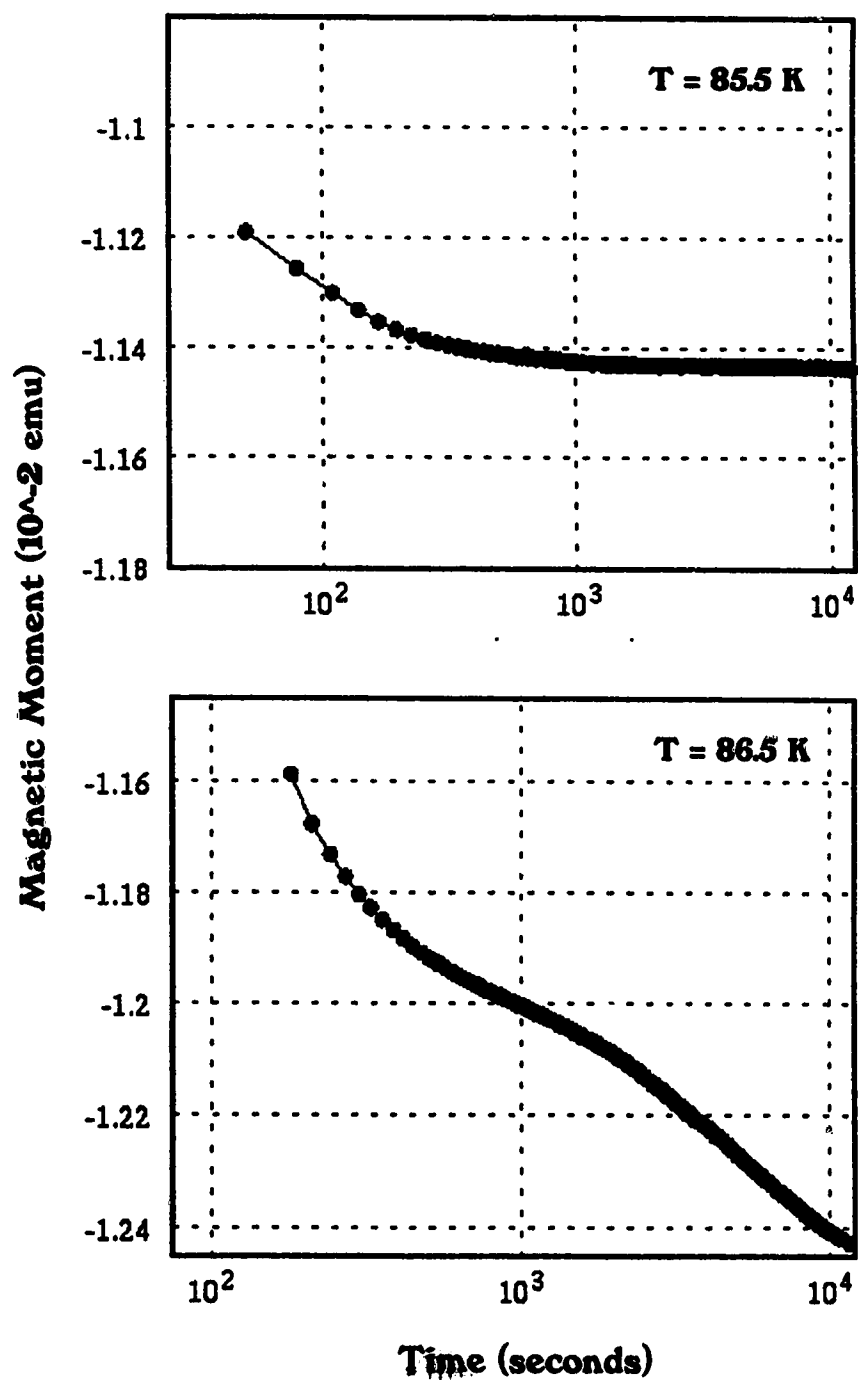


Figure 2.8: Magnetic moment as a function of time in the field - cooled $YBa_2Cu_3O_{7-x}$ sample (RJJ1A) at 5 G. The temperature of the measurements is 85.5 and 86.5 K.

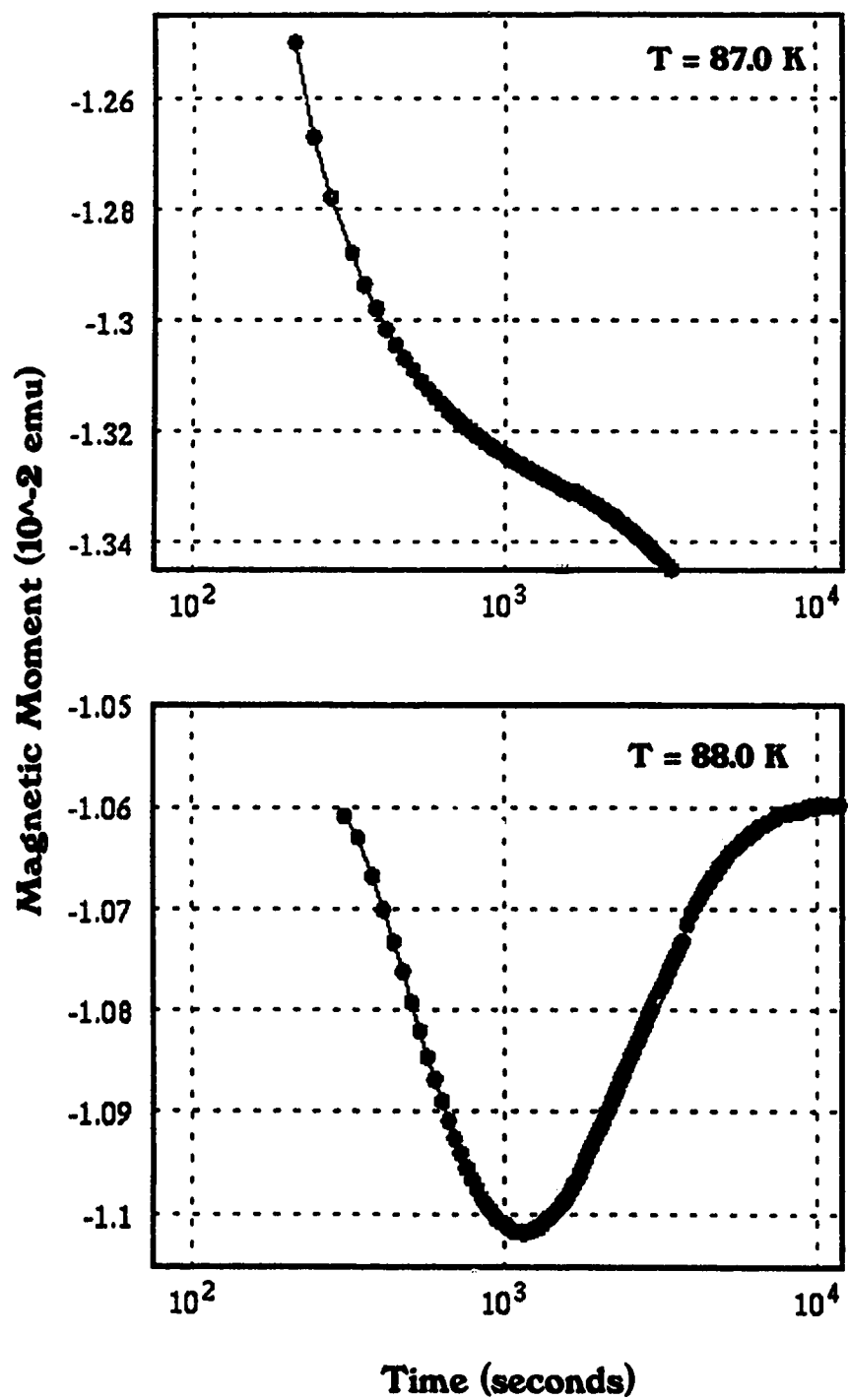


Figure 2.9: *Magnetic moment as a function of time in the field - cooled $\text{YBa}_2\text{Cu}_3\text{O}_{7-x}$ sample (RJJ1A) at 5 G. The temperature of the measurements is 87.5 and 88.0 K.*

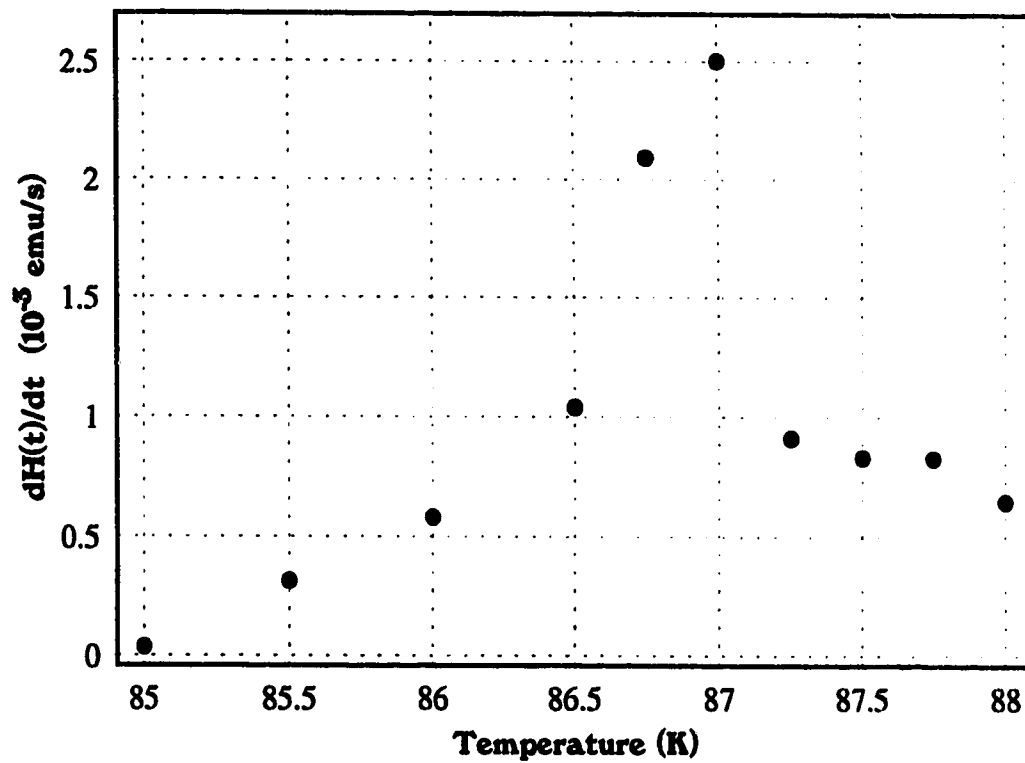


Figure 2.10: *The Meissner moment increase rate measured on the $\text{YBa}_2\text{Cu}_3\text{O}_{7-x}$ sample (RJJ1A) versus temperature in an applied field of 5 G.*

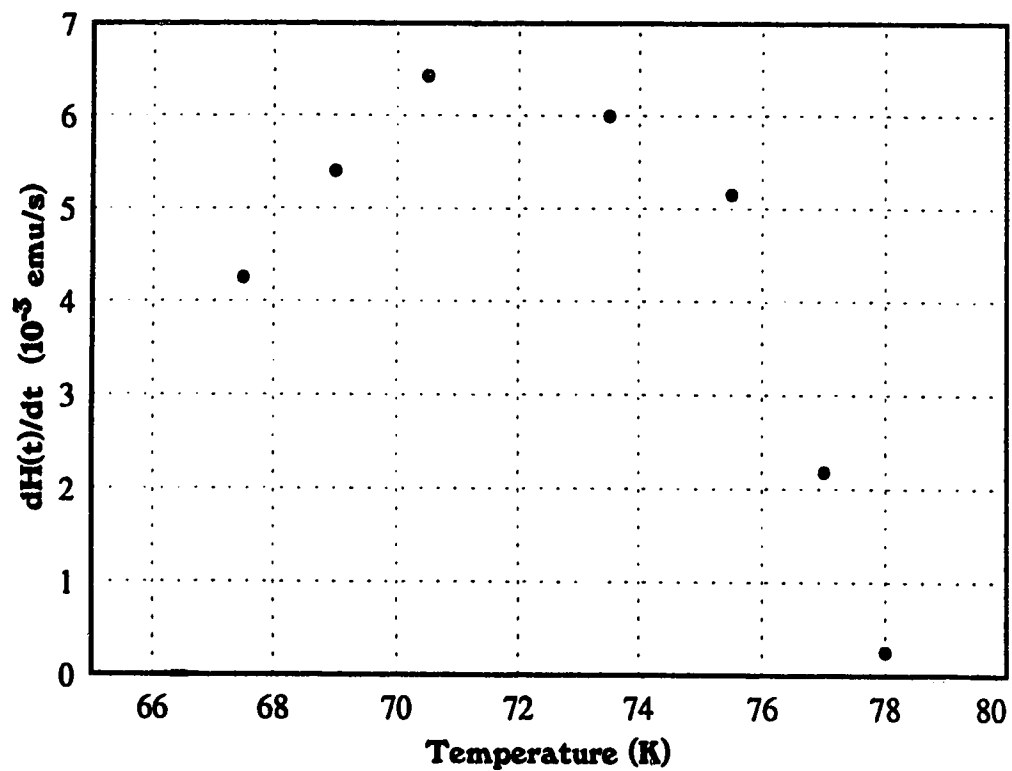


Figure 2.11: *The Meissner moment increase rate measured on the $YBa_2Cu_3O_{7-x}$ sample (RJJ1A) versus temperature in an applied field of 100 G.*

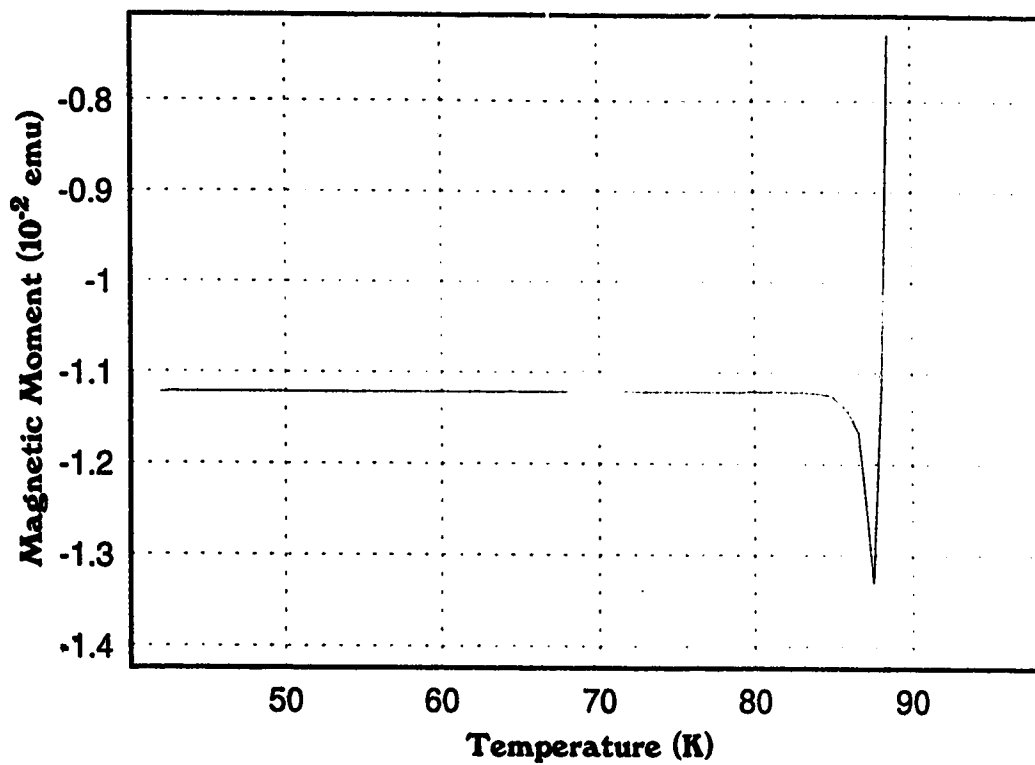


Figure 2.12: *Magnetic moment vs. temperature measurements of the $YBa_2Cu_3O_{7-x}$ sample in an applied field of 5 G.*

temperatures below T_c of the grains.

2.7 Discussion

a) Pinning Effects

The $\text{YBa}_2\text{Cu}_3\text{O}_{7-x}$ (RNG9), $\text{YBa}_2\text{Cu}_3\text{O}_{7-x} + \text{Ag}$ (2% wt.) (RNG6), and $\text{YBa}_2\text{Cu}_3\text{O}_{7-x} + \text{Ag}$ (4% wt.) (RNG10) samples have been measured in a FCI procedure using applied fields of 5 to 900 G. Fig. 2.13 shows the FCI data of each sample in an applied field of 20 G. The pure sample (dotted line) exhibits a sharp transition in the mag-

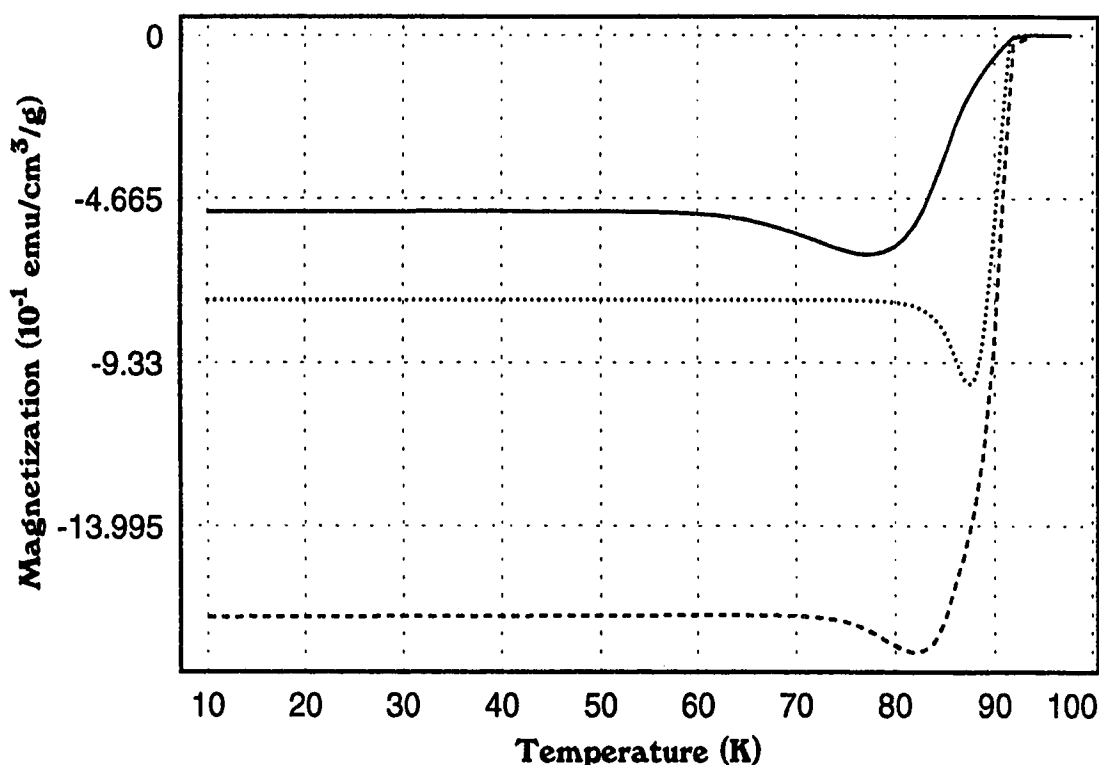


Figure 2.13: FCI measurements (fast cooling) on $\text{YBa}_2\text{Cu}_3\text{O}_{7-x}$ (RNG9) (dotted line), $\text{YBa}_2\text{Cu}_3\text{O}_{7-x} + \text{Ag}$ (2% wt.) (RNG6) (solid line) and $\text{YBa}_2\text{Cu}_3\text{O}_{7-x} + \text{Ag}$ (4% wt.) (RNG10) (dashed line) in an applied field of 20 G.

netic moment from T_d to T_c . The width of this transition from the superconducting

to normal phases is indicative of the sample's quality as a large fraction of the sample remains superconducting to temperatures close to T_c . Accordingly, the transition widths of the silver doped samples are broader allowing the penetration of flux and reduction of superconducting regions over a wider range of temperatures.

The $\text{YBa}_2\text{Cu}_3\text{O}_{7-x} + \text{Ag}$ (2% wt.) (RNG6) sample (solid line) traps more flux than pure $\text{YBa}_2\text{Cu}_3\text{O}_{7-x}$ (RNG9). The silver in this case must be offering more pin sites for the penetrating flux. Yet the temperature of the onset of flux expulsion is much lower indicating that the pinning forces are weaker than those of $\text{YBa}_2\text{Cu}_3\text{O}_{7-x}$ (RNG9). The temperature range in which flux depinning and the flow of flux occurs is also wider. The $\text{YBa}_2\text{Cu}_3\text{O}_{7-x} + \text{Ag}$ (4% wt.) (RNG10) sample (dashed line) on the other hand traps less field than either the pure sample or the 2% silver doped sample. In this case, it seems that the silver, which coats the grains more uniformly is affecting the amount of intergrain flux trapping. The temperature range in which depinning occurs is also extended and the transition width spread when compared to the pure $\text{YBa}_2\text{Cu}_3\text{O}_{7-x}$ (RNG9) results.

The magnetization of the two pure $\text{YBa}_2\text{Cu}_3\text{O}_{7-x}$ ceramic samples (RJJ1A and RNG9) of different sizes were measured. Sample RJJ1A (solid line) has larger weight and shows slightly higher magnetization when measured with the FCI procedure (Fig. 2.14). With the pure samples, the transition widths are sharp, the temperature range where depinning occurs is small, and the onset temperature is high due to the good quality of the samples.

b) Field Versus Temperature Phase Diagrams

By plotting the onset and completion temperatures dependent on applied magnetic field for each sample, phase diagrams are drawn in the (H,T) plane. The phase diagram depicts the intergrain flux depinning characteristic of each sample. Fig. 2.15

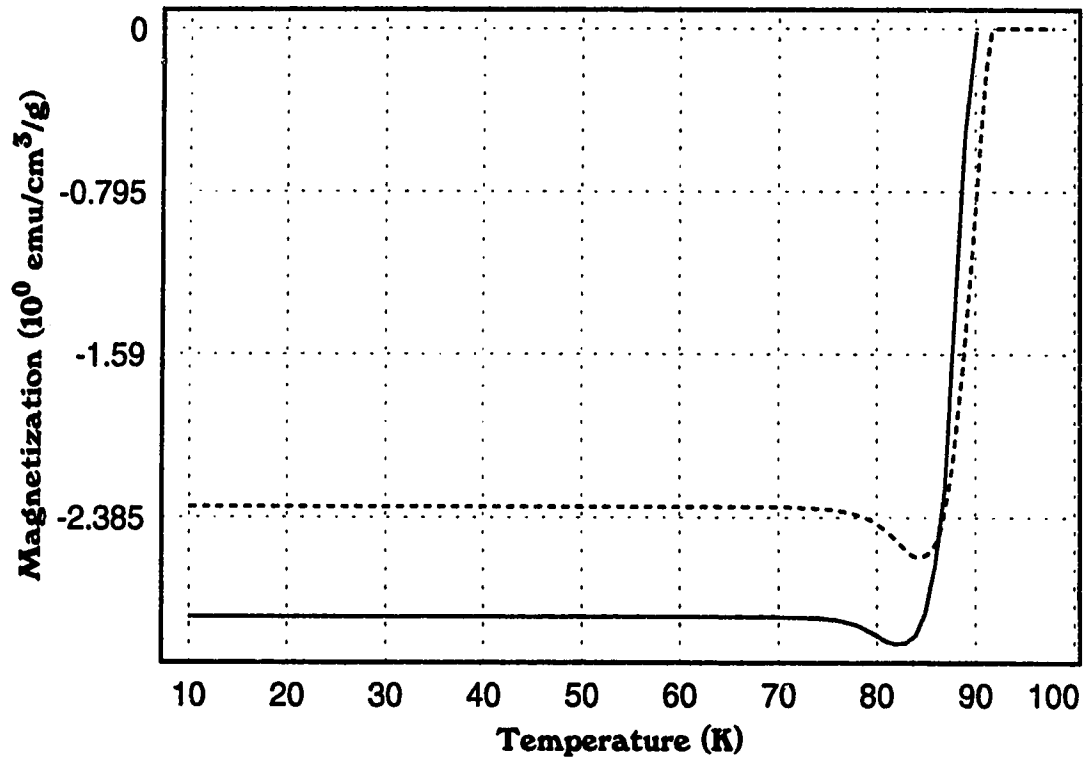


Figure 2.14: FCI measurements on samples $YBa_2Cu_3O_{7-x}$ (RNG9) (dashed line) and RJJ1A (solid line) in an applied field of 40 G.

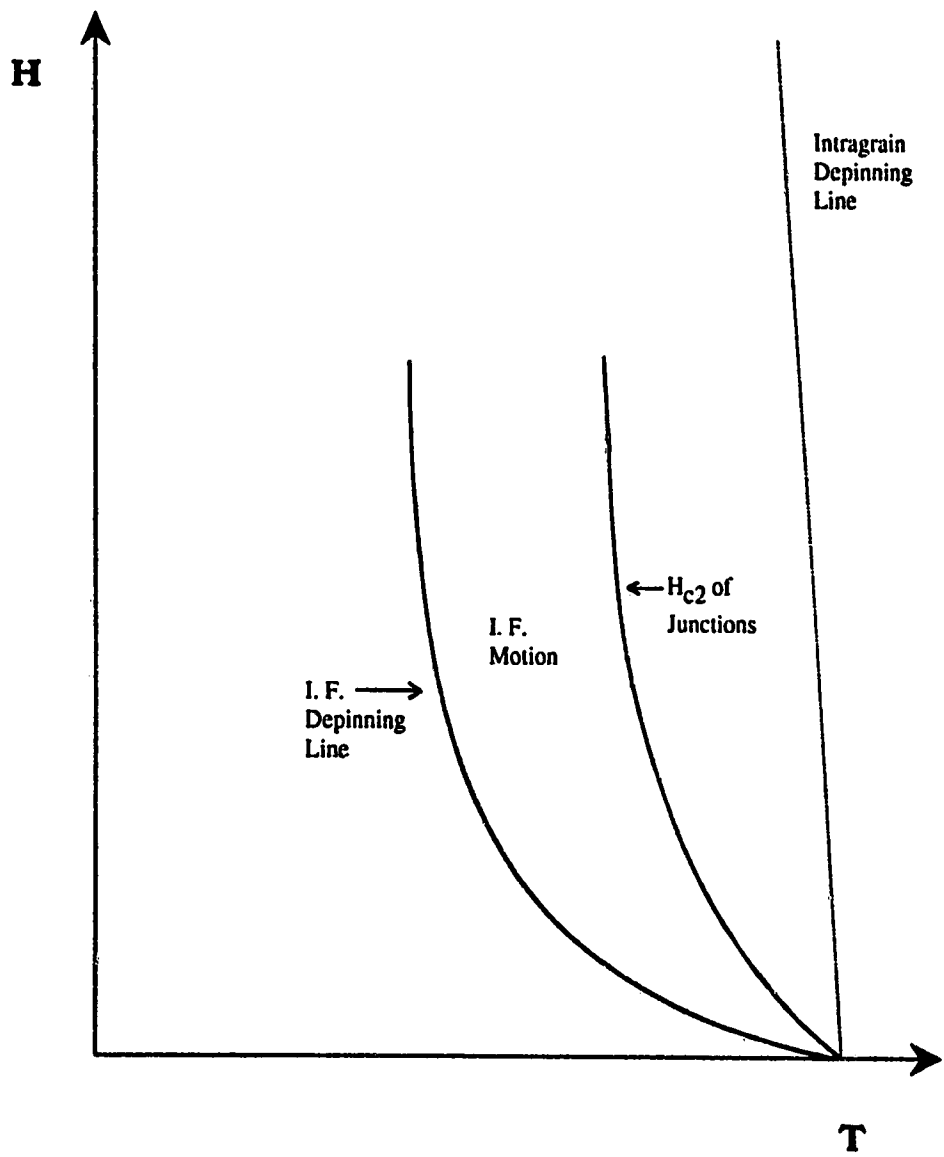


Figure 2.15: *General phase diagram of applied field versus temperature for ceramic superconducting samples. I. F. refers to intergrain flux.*

shows the general phase diagram which describes the intergrain flux behaviour of the samples.

Depinning Onset Temperatures T_0

Higher onset temperatures indicate stronger pinning at the intergrain junctions since the thermal energy needed to depin the flux is greater. The pinning in the $\text{YBa}_2\text{Cu}_3\text{O}_{7-x}$ + Ag (2% wt.) (RNG6) sample is significantly weaker than the pure sample. This is evident in Fig. 2.16 where the onset temperatures form phase lines which determine when the intergranular flux initially becomes depinned. The line for the $\text{YBa}_2\text{Cu}_3\text{O}_{7-x}$ + Ag (2% wt.) sample (RNG6) (triangles) is shifted to lower temperatures in comparison to those of $\text{YBa}_2\text{Cu}_3\text{O}_{7-x}$ (RNG9) (X's). In higher applied fields (400 G and up) the onset temperatures of both samples are comparable.

Throughout the applied fields up to 400 G, the $\text{YBa}_2\text{Cu}_3\text{O}_{7-x}$ + Ag (4% wt.) sample (RNG10) (circles) has noticeably higher onset temperatures than the $\text{YBa}_2\text{Cu}_3\text{O}_{7-x}$ + Ag (2% wt.) sample (RNG6). The addition of 4% silver per sample weight has affected the pinning strength of the trapped flux. The amount of flux trapped and its pinning depends significantly on the intergrain junction characteristics.

The increase in the magnetic moment due to intergranular depinning becomes less prominent with higher applied fields. Samples $\text{YBa}_2\text{Cu}_3\text{O}_{7-x}$ + Ag (2% wt.) (RNG6) and $\text{YBa}_2\text{Cu}_3\text{O}_{7-x}$ (RNG9) demonstrate this property up to applied field of 900 G. $\text{YBa}_2\text{Cu}_3\text{O}_{7-x}$ + Ag (4% wt.) sample (RNG10), however, loses this characteristic around 350 G.

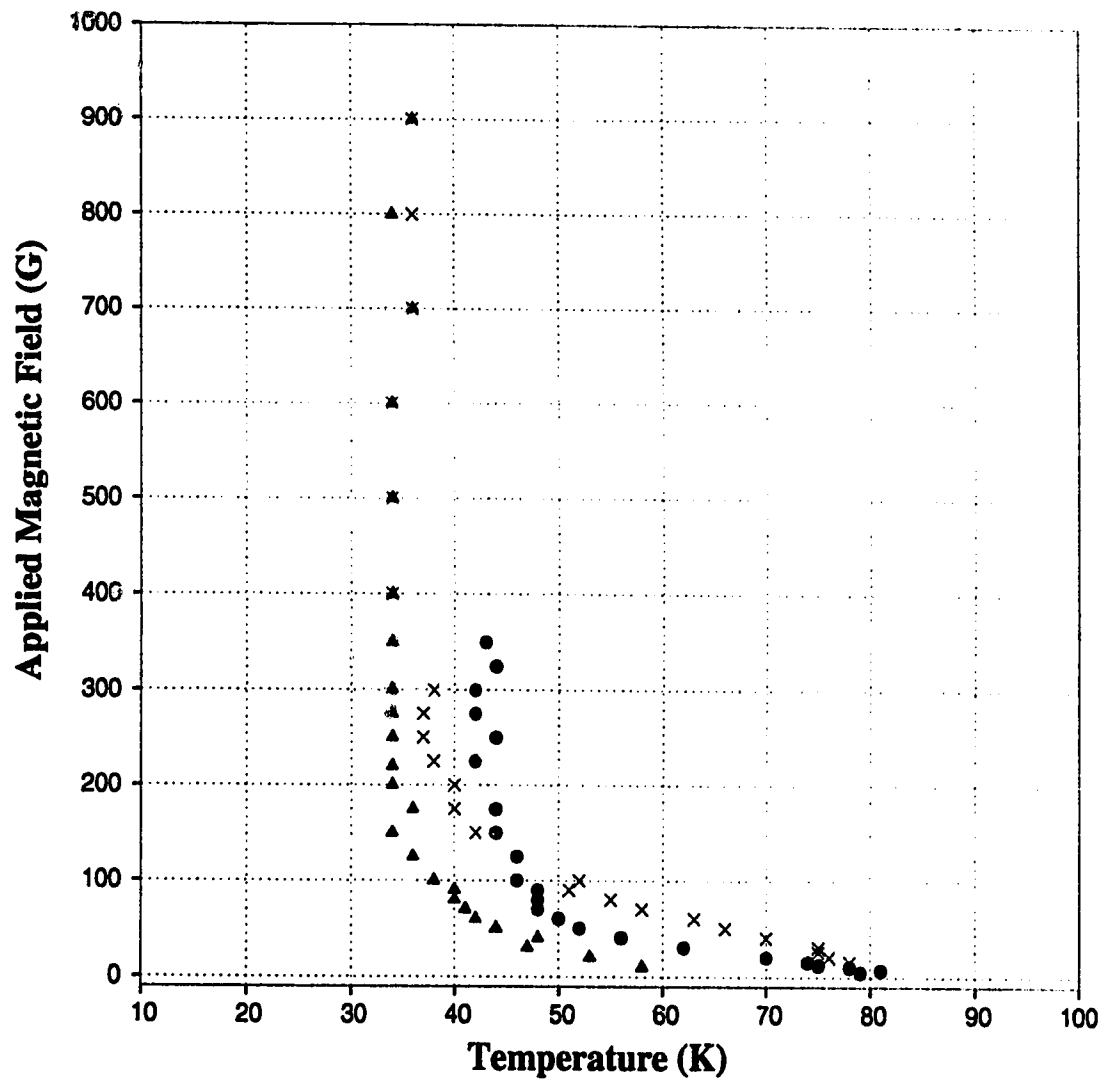


Figure 2.16: Phase diagram of applied field versus onset temperature for samples $\text{YBa}_2\text{Cu}_3\text{O}_{7-x}$ (RNG9) (X's), $\text{YBa}_2\text{Cu}_3\text{O}_{7-x} + \text{Ag}$ (2% wt.) (RNG6) (triangles) and $\text{YBa}_2\text{Cu}_3\text{O}_{7-x} + \text{Ag}$ (4% wt.) (RNG10) (circles).

Depinning Completion Temperatures T_d

The temperature where the depinning processes are overcome by the moving of flux into the sample is called the completion temperature (T_d). The completion temperatures form a phase diagram in the (H,T) plane and is discussed for each sample. Fig. 2.17 shows that the pure sample, (RNG9) (X's in Fig. 2.17), has consistently higher completion temperatures for all values of applied field than the $\text{YBa}_2\text{Cu}_3\text{O}_{7-x} + \text{Ag}$ (2% wt.) sample (RNG6) (triangles in Fig. 2.17). The phase line for the pure sample is linear from 7 to 150 G as T_d decreases with increasing field. As the applied field is varied over a large range from 150 to 900 G, T_d changes slowly.

The $\text{YBa}_2\text{Cu}_3\text{O}_{7-x} + \text{Ag}$ (2% wt.) sample (RNG6) shows similar behavior to the pure sample. The depinning temperatures indicating the motion of flux into the sample and decoupling of grains is at temperatures lower than those exhibited by the pure sample. The linearity of the phase line for $\text{YBa}_2\text{Cu}_3\text{O}_{7-x} + \text{Ag}$ (2% wt.) sample (RNG6) exists up to an applied field of 100 G.

The $\text{YBa}_2\text{Cu}_3\text{O}_{7-x} + \text{Ag}$ (4% wt.) sample (RNG10) reveals an interesting behavior in this phase diagram. T_d for this sample is higher than that of the $\text{YBa}_2\text{Cu}_3\text{O}_{7-x} + \text{Ag}$ (2% wt.) sample (RNG6) in very low applied fields ($H_a < 50$ G). The completion temperatures, however, drop faster with increasing field than either the $\text{YBa}_2\text{Cu}_3\text{O}_{7-x} + \text{Ag}$ (2% wt.) (RNG6) or $\text{YBa}_2\text{Cu}_3\text{O}_{7-x}$ (RNG9) samples. This suggests the low field properties of the $\text{YBa}_2\text{Cu}_3\text{O}_{7-x} + \text{Ag}$ (4% wt.) sample (RNG10) are such that the pinning is stronger and the penetration of flux is prevented until higher temperatures are achieved. The H vs. T_d line quickly drops to similar values to those for the $\text{YBa}_2\text{Cu}_3\text{O}_{7-x} + \text{Ag}$ (2% wt.) sample (RNG6) applied field is increased. Observable depinning of intergrain flux is absent, at least to within sensitivity of the measurements, in $\text{YBa}_2\text{Cu}_3\text{O}_{7-x} + \text{Ag}$ (4% wt.) sample (RNG10) for fields above 350 G.

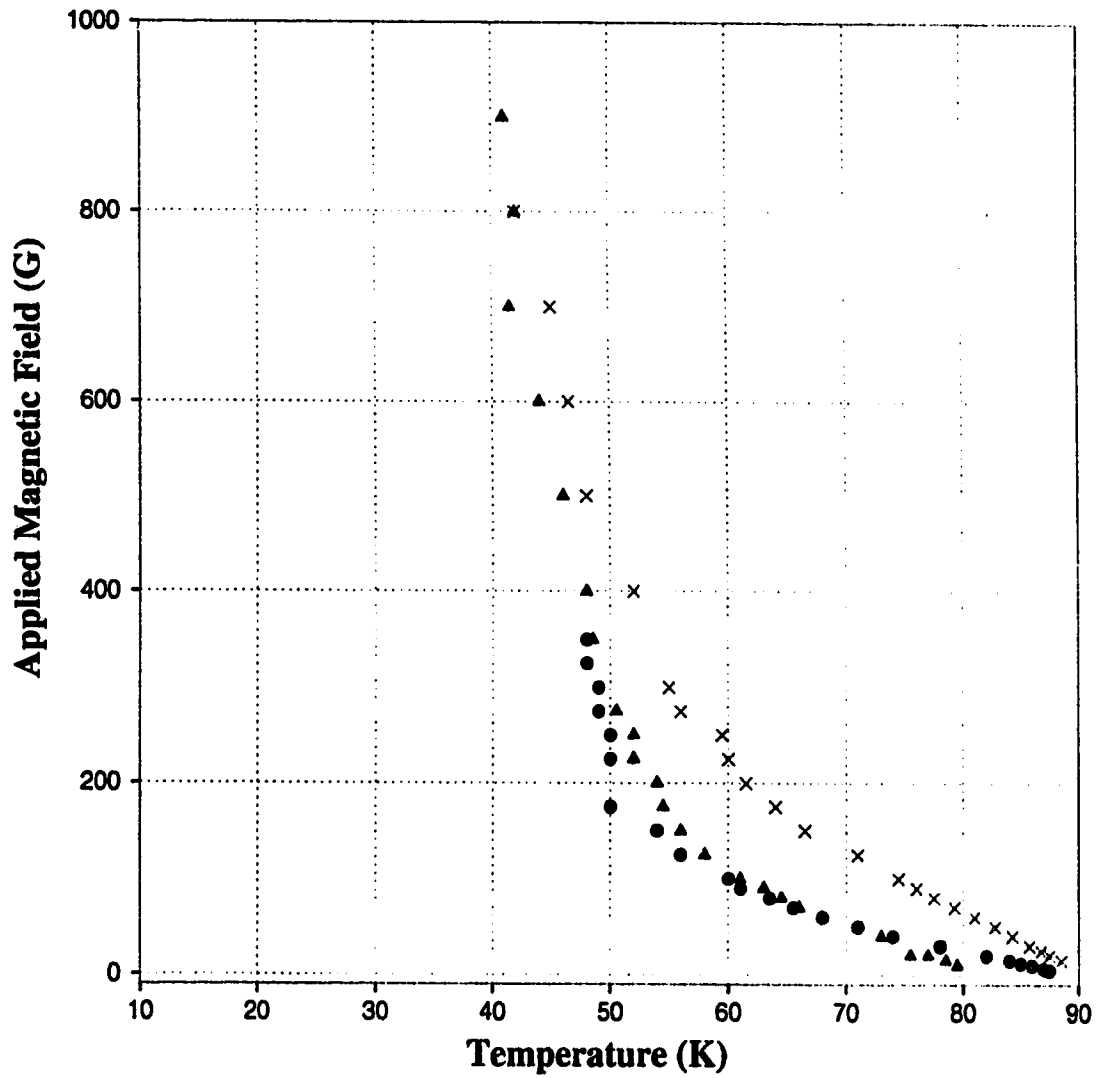


Figure 2.17: Phase diagram of applied field versus depinning completion temperatures for samples $YBa_2Cu_3O_{7-x}$ (RNG9) (X's), $YBa_2Cu_3O_{7-x} + Ag$ (2% wt.) sample (RNG6) (triangles) and $YBa_2Cu_3O_{7-x} + Ag$ (4% wt.) sample (RNG10) (circles).

No effect on the phase diagram due to sample size is seen. The phase lines of the pure samples RJJ1A and RNG9 are compared in figure 2.18 and are mostly coincident. The obvious difference is the magnitude of applied field in which the depinning of intergrain flux lines is suppressed. For $\text{YBa}_2\text{Cu}_3\text{O}_{7-x}$ (RNG9) this field is 900 G. For the larger sample, RJJ1A, this field is 1800 G.

Also displayed in Fig. 2.18 is the irreversibility line measured from a rod shaped pressed - powder sample of pure $\text{YBa}_2\text{Cu}_3\text{O}_{7-x}$. This line is determined by applied magnetic fields and temperatures where ZFC and FC magnetic moments coincide, and represents the intragranular flux depinning. The irreversibility line is at significantly higher temperatures and higher fields than the intergranular flux depinning phase lines. This indicates that the intragrain pinning is much stronger than the intergrain pinning.

The intergrain depinning lines of the samples with 2% Ag (wt.) added (RAJJ1 and RNG6) are shown in Fig. 2.19 showing the reproducibility of the phase diagrams.

Phase Diagram at Very Low Applied Fields

Magnetization measurements were performed at very low applied fields using the pure $\text{YBa}_2\text{Cu}_3\text{O}_{7-x}$ sample (RJJ1A). Closer analysis of the phase diagram shows an interesting characteristic (Fig. 2.20). For applied fields below 5 G, T_d remains constant at 87.5 K. This implies that 87.5 K is the highest T_d achieved by this sample below 5 G before the processes reducing the sample's magnetization (flux in) overcome the processes increasing the magnetization (flux out). Above T_d , the motion of flux into the sample occurs at a much more rapid rate than the expulsion of flux. The flux penetration is a likely result of the decoupling of intergrain junctions and destruction of intergrain currents. Thus the temperature 87.5 K appears to be related to the critical temperature of the transport current when the applied field is less than 5 G.

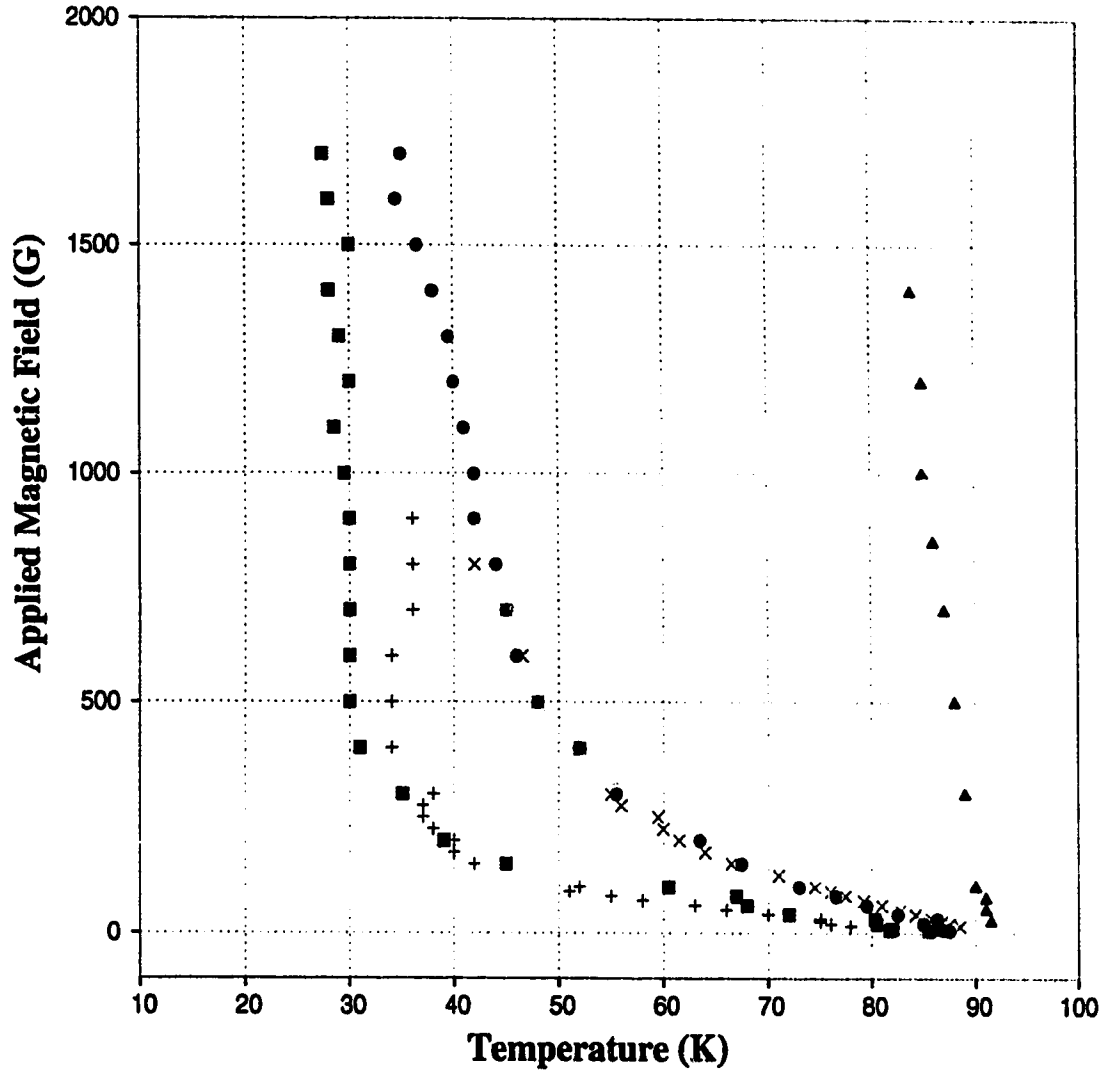


Figure 2.18: Phase diagram of applied field versus the onset of depinning and depinning completion temperatures for the pure $\text{YBa}_2\text{Cu}_3\text{O}_{7-x}$ samples RNG9 (X,+) and RJJ1A (squares,circles). The irreversibility line for intragranular depinning measured on the pressed - powder $\text{YBa}_2\text{Cu}_3\text{O}_{7-x}$ sample RBJJ1 [32] is given by the triangles. RBJJ1 exhibited intergrain depinning before the pulverizing procedure.

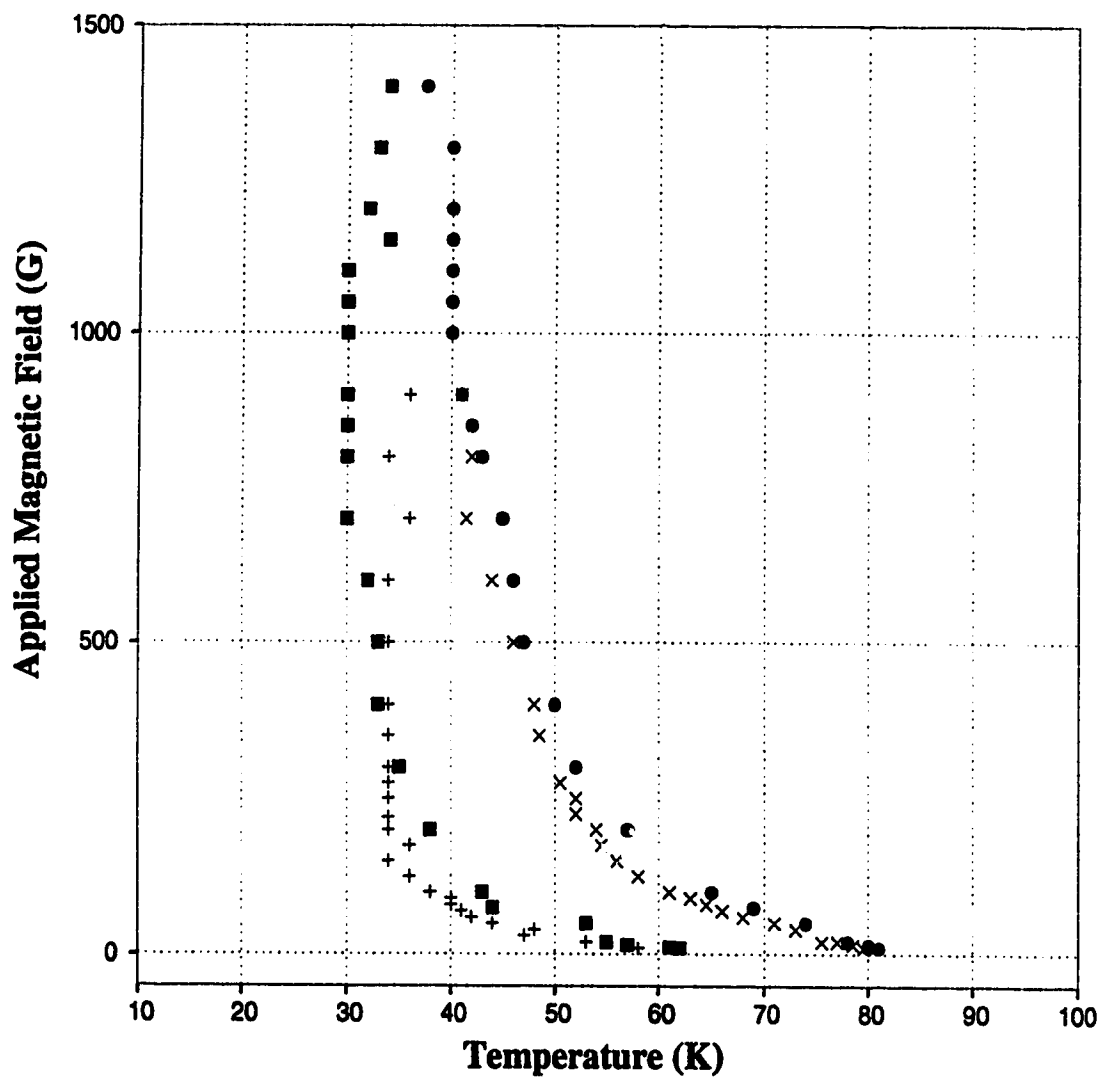


Figure 2.19: Phase diagram of applied field versus the onset of depinning and depinning completion temperatures for the $\text{YBa}_2\text{Cu}_3\text{O}_{7-x} + 2\% \text{ Ag}$ (wt.) samples RNG6 (X,+) and RAJJ1 (squares,circles).

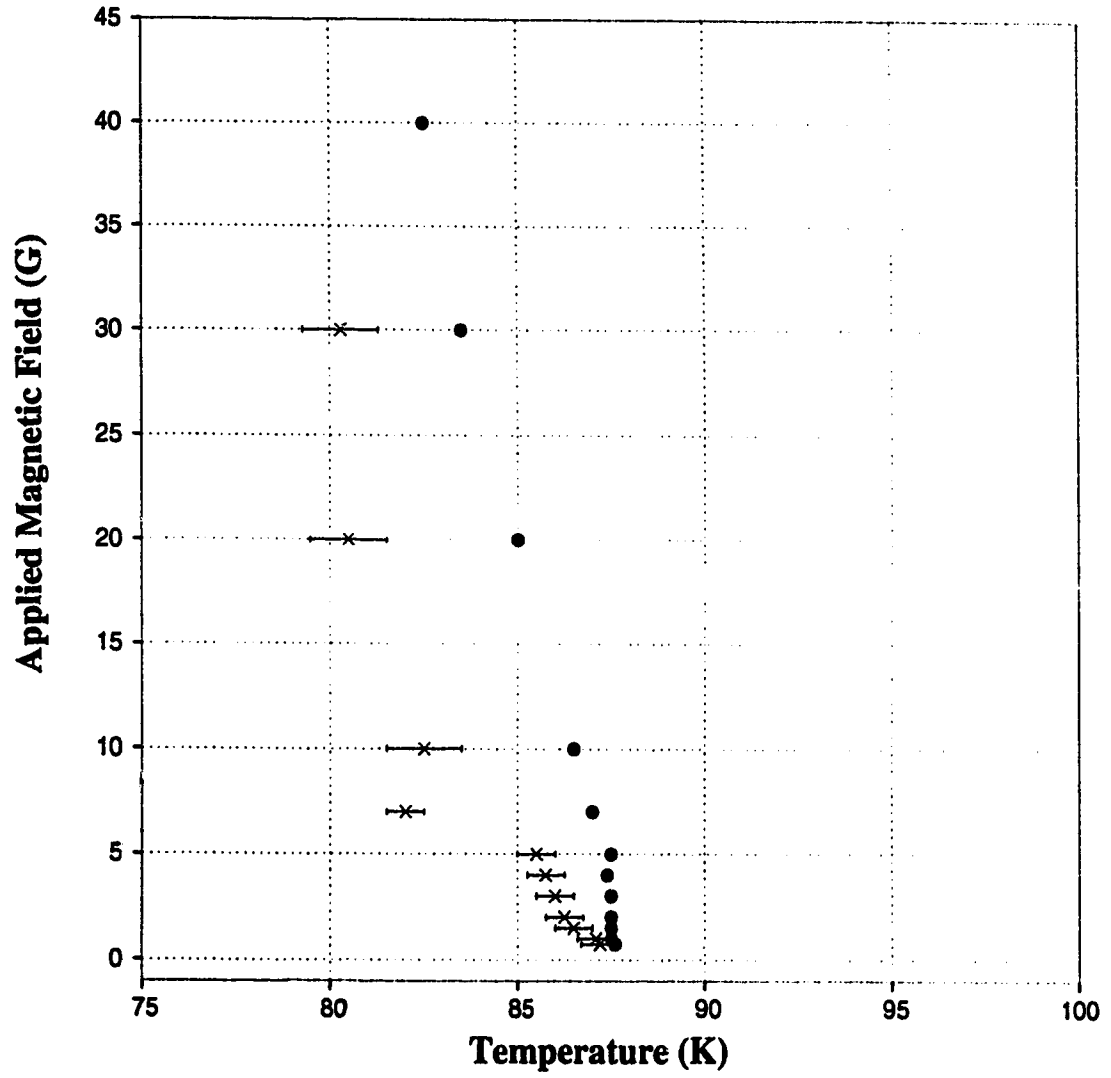


Figure 2.20: *Phase diagram of applied field versus onset of depinning and depinning completion temperatures for the pure $\text{YBa}_2\text{Cu}_3\text{O}_{7-x}$ sample RJJ1A.*

CHAPTER THREE

EXTENDED CRITICAL STATE MODEL FOR A DISK SHAPED TYPE II SUPERCONDUCTOR

3.1 Introduction

As introduced by Bean [31], the critical-state model has proven itself useful in determining the diamagnetic shielding behavior and critical current distributions of a variety of superconducting samples and sample shapes. This model suggests a sample responds to any change in an applied magnetic field by setting up shielding currents that flow at the level of a critical current density J_c . These currents and their distributions will depend on the magnitude of the applied field and the local fields within the sample, $J = J_c(B)$. Previous applications [31, 32] to slab and cylindrical geometries were done where it was approximated that there was no dependence of the critical current on the magnetic fields; $J_c(B) = \text{const}$. Further studies using disk - shaped geometries and where the currents were assumed field dependent were completed and discussed [33, 34]. In these studies, the trapped flux and magnetic shielding behavior and critical currents of disk-shaped samples were modelled and compared to experiment.

The critical state Bean model is a method of determining the critical currents of superconducting samples. These critical currents are the macroscopic transport currents flowing through the sample. For granular superconductors, the macroscopic currents are dependent upon the intergrain junctions and their behavior in magnetic fields. Furthermore, currents on the individual grains themselves will flow. These currents also contribute to the sample's shielding capabilities.

The present work extends this discussion to a disk-shaped high temperature ceramic type II superconductor. Special considerations must be made since the shielding currents in such samples are not solely composed of the intergranular critical currents (transport currents dealt with in the Bean model), but also include intragranular currents [35, 36]. Demagnetization due to the sample shape is in fact a large and noteworthy consideration. The application of an extended critical state model, which takes into account the intragrain, intergrain currents and demagnetization effects, as applied to ceramic samples is discussed.

3.2 Bean Model of Critical-State Superconductors

Magnetization measurements of superconducting samples give a basic understanding of the nature of superconductivity. An important discovery, being the Meissner effect; ie. the total expulsion of all magnetic flux from a sample, gave an idea of the characteristics of superconducting samples; perfect diamagnetism. The properties of type II superconductors allow for magnetic flux penetration into samples over a broad range of applied magnetic field without destroying superconducting currents. Abrikosov [6] laid the groundwork for understanding this phenomenon. Abrikosov's theory allows for magnetic flux to enter samples in the form of magnetic flux quanta. The penetration begins at a low applied field denoted by H_{c1} , and continues to enter the sample till superconductivity is quenched at H_{c2} . The sample is said to be in a *mixed state* within this applied field range.

Bean [31] proposed a model, the critical-state model, to describe the magnetic and electrical behavior of a superconducting sample in the mixed state. This model proposes the existence of a macroscopic superconducting critical current density whose magnitude is a maximum value dependent on the local magnetic field. The critical current arises as a consequence of Ampere's law: $\vec{\nabla} \times \vec{H} = \mu_0 \vec{J}$, ie. a gradient of flux lines exists as flux enters the sample into a mixed state. The initial stages of

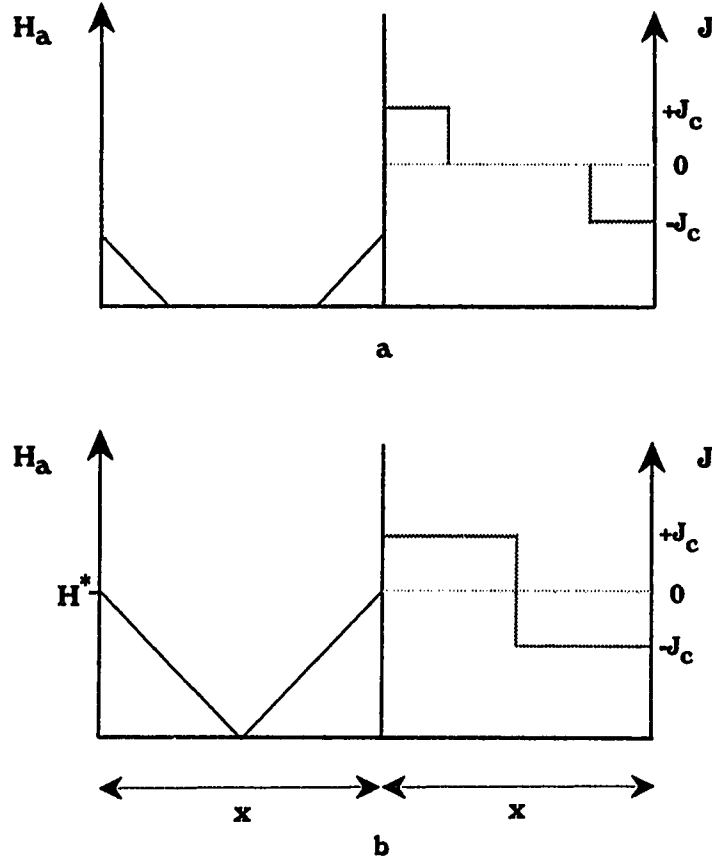


Figure 3.1: *Illustration of Bean's model. Local fields and current density for applied fields parallel to the surface of a slab of thickness x . a) applied field is less than H^* and b) applied field is H^* as entire sample is in the critical state.*

the magnetization, occurring when the applied magnetic field is increased above H_{c1} , is characterized by shielding currents beginning to flow at the critical current level in a layer of thickness dependent on the local magnetic field's magnitude. When the applied magnetic field is low, the flux line gradients will not penetrate through the entire sample. As a result, the interior of the sample unaffected by the flux will have no currents induced and the current density will be zero (Fig. 3.1 a). The shielding currents will flow at the sample surface such that the internal local magnetic field is reduced to zero. As the external applied field is increased, the shielding currents flow in an increasing volume of the sample till a field, H^* , is reached whereby the entire

sample is in the critical state (Fig. 3.1 a). For modelling purposes a uniform current density has been used, but a field dependent J_c yielded a unique spatial dependence as the local fields affecting each grain junction and thus the intergrain currents. In fact, the induced self-fields of the shielding currents superposed with the applied field within the sample are used to limit the critical current magnitude, $J_c(B)$.

This model has been successfully applied to various superconducting samples and sample shapes [37]. The treatment allows for the connection between microscopic pinning forces, the critical current density, and the observed macroscopic magnetic measurements.

3.3 Granular Superconductors

Determining the characteristics of ceramic superconducting samples is quite difficult due to the inhomogeneous anisotropic structures of the materials. Such inhomogeneity can be the direct result of the fabrication of the material or as in the case of polycrystalline ceramic superconductors, can also be an intricate component of its nature. Since their recent discovery [38], extensive research on the critical current of such ceramic samples, in particular $\text{YBa}_2\text{Cu}_3\text{O}_{7-x}$, has been done. Inductive measurements [39, 40] have shown the current carrying capacities of these superconductors are two-fold. Localized intragrain currents flowing within individual grains exist and may have very large magnitudes (of the order of $10^7 \frac{\text{A}}{\text{cm}^2}$). These currents depend on flux-line pinning on twin boundaries or impurities within the sample grains. In addition to these intragrain currents a macroscopic transport current flows throughout the sample.

The transport (intergrain) current traverses the sample by passing through the weak superconducting links between grains. These weak links, forming a weak link network, consist of normal or insulating barriers due primarily to poor stoichiometry

or impurities, crystallographic changes between grains, geometric constraints or to twin boundaries and defects within the grains themselves. The ability of such weak links to pass a supercurrent depends strongly on the local magnetic field, both its direction and magnitude. The directional dependence of an entire sample can be taken as an average contribution from the weak link network since, as an applied field is rotated, the allowable current through one weak link is suppressed while another may be increased. This effect would change the spatial distribution of the allowed currents but as suggested above and discussed below an averaging treatment would be adequate in describing the system on the sample scale.

The actual tunneling mechanism through the weak links and the resulting magnetic dependence on the transport critical current, $J_c(B)$ is of importance when studying properties of ceramic superconductors. Consider an individual weak link; since the fundamental concepts of the Josephson effect can be applied to any type of superconducting - insulating - superconducting weak link, the tunneling of superconducting electrons is described by Josephson tunneling processes. This means that a magnetic field which has penetrated the barrier between grains will tend to quickly reduce the tunneling current. The junctions can be adequately described by the known Josephson equations [2, 41]. As discussed by Peterson and Ekin [42], the current carrying ability of a junction depends upon the dimensions of the junction and the Josephson penetration length λ_J , which is defined as $\lambda_J^2 = \frac{\phi_0}{2\pi\mu d J_c(0)}$. Here μ is the permeability of the junction and ϕ_0 is the flux quantum. When λ_J is larger than the width of the junction the contributions from intragrain defects and twin boundaries can be discarded. The current through the junction is considered uniform and the following relation between the critical current and magnetic field holds:

$$J_c(B, r) = J_c(0) \frac{\sin\left(\frac{\pi B(r)}{B_0}\right)}{\left(\frac{\pi B(r)}{B_0}\right)} \quad (3.1)$$

Peterson and Ekin [42] use this relation along with a statistical averaging over junction

dimensions to describe the critical current dependence in a granular superconductor on magnetic field. The result of their work adequately describes the transport current density of the granular samples.

3.4 Type II Superconductors in the Critical-State

First applications of a critical state model to type II superconductors were done by Frankel [33]. Frankel calculated the resulting axial magnetic shielding field of a disk-shaped sample of NbTi in an axially applied field. The shielding was calculated taking a model disk filled with concentric current loops flowing at the critical current level with magnetic field dependence as determined by Kim's relation [32]. Magnetic dependence of J_c was included by iterative procedures. This work was extended by Däumling and Larbalestier for disks of different aspect ratios (the ratio of sample radius to sample thickness r_0/d). Furthermore, their calculations gave both axial and radial magnetic shielding fields. Däumling and Larbalestier have concluded that the shielding field of their sample depends on the thickness of the sample rather than the sample radius, ie. the shielding field is proportional to $J_c d$. Also, it was noted that there exists a substantial radial field not present in the long cylindrical geometries.

The samples considered by Frankel and by Däumling and Larbalestier were conventional superconductors *NbTi* and *Nb₃Sn* respectively. Important differences exist between such superconductors and the *YBa₂Cu₃O_{7-x}* superconductor. Firstly, the magnitude of the critical transport currents in the niobium based superconductors are substantially higher. The low critical current density, due to the intergranular weak links of the *YBa₂Cu₃O_{7-x}* ceramic sample, will greatly affect the results of the conventional Bean model. The demagnetization effects, flux penetration, flux flow, and the intragrain contributions to the shielding field have greater importance due to the intrinsic characteristics of *YBa₂Cu₃O_{7-x}* ceramic samples.

Due to the fact that the magnetization and applied magnetic field point in opposite directions in a sample of finite dimensions, demagnetization effects become important. The demagnetization field depends on two factors; the magnetization of the material and the geometry of the sample. To find the internal field of a sample of finite size in an applied magnetic field, corrections due to the demagnetization field are always necessary. Demagnetization factors are analytically solved for spheres and ellipsoids but cannot be for solids of various other shapes including disks.

At low applied magnetic fields, $H_a < H^*$, the demagnetization effects and intergrain flux penetration play an integral part in determining the distribution of the shielding currents. Often a fraction of the sample may not be carrying shielding currents leaving it in a partial critical state. Following the ideas of Bean [31], a critical current distribution will be induced in order to shield the sample from the applied field. This current distribution will initially be limited to a thin layer starting at the outer edges of the sample. It should be noted that simultaneously, current densities of significantly larger magnitudes will flow on the superconducting grain surfaces in addition to the shielding currents. As the applied field increases, the fraction of the sample carrying the shielding current distribution also increases till the field, H^* , is reached whereby the sample is totally in the critical state.

While the applied field is increased, more flux will penetrate the sample edges in the form of Josephson vortices or intergrain vortices. Further increases of the applied field will result in flux gradients large enough to depin the intergranular flux. The intergrain flux flow will dissipate the superconducting shielding currents in the disk edges resulting in new critical current distributions within the sample.

Shielding field profiles were measured using a Hall probe including the dependence of shielding versus applied field at different points along the diameter of a $\text{YBa}_2\text{Cu}_3\text{O}_{7-x}$ ceramic disk [43]. The objective of the present work was to compare this data with computer calculations and fits to the shielding field profiles and ver-

ify the effect of the demagnetization factors, flux flow and intergrain and intragrain critical currents.

3.5 Critical-State Model

a) *Critical-State Model for a Disk-Shaped Sample*

To determine shielding field profiles across the diameter of a disk shaped superconductor in the critical state requires a knowledge of the magnitude of the local magnetic field gradients. They could be found with the application of elementary electromagnetic theory. In the case of a disk in an applied axial field, the critical currents are strictly azimuthal. This comes as the relation $\mu_0 \vec{J} = \vec{\nabla} \times \vec{B}$ is substantially reduced to

$$\mu_0 J_\phi = \left(\frac{\partial B_r}{\partial z} \right) - \left(\frac{\partial B_z}{\partial r} \right). \quad (3.2)$$

Equation (3.2) is in cylindrical coordinates, r is the radial component, z , the axial component, and ϕ is the azimuthal component. B_r is the radial component of the magnetic field and B_z is the axial component. J_ϕ is the only contributing (aximuthal) component of the critical currents.

The sample may be considered to be composed of thin disks of concentric current loops, see Fig. 3.2. The calculation of the magnetic field at arbitrary points above and within the sample is then the superposition of the magnetic fields due to each current loop. The z and r components of the field at position (r, z) (z is the height above the specific loop considered) due to one current loop of radius r_i is given by [44]

$$B_z(r, z) = \frac{\mu_0 I}{2\pi} \frac{1}{\{(r + r_i)^2 + z^2\}^{\frac{1}{2}}} \left[K(k) + \frac{r^2 - r_i^2 - z^2}{(r - r_i)^2 + z^2} E(k) \right],$$

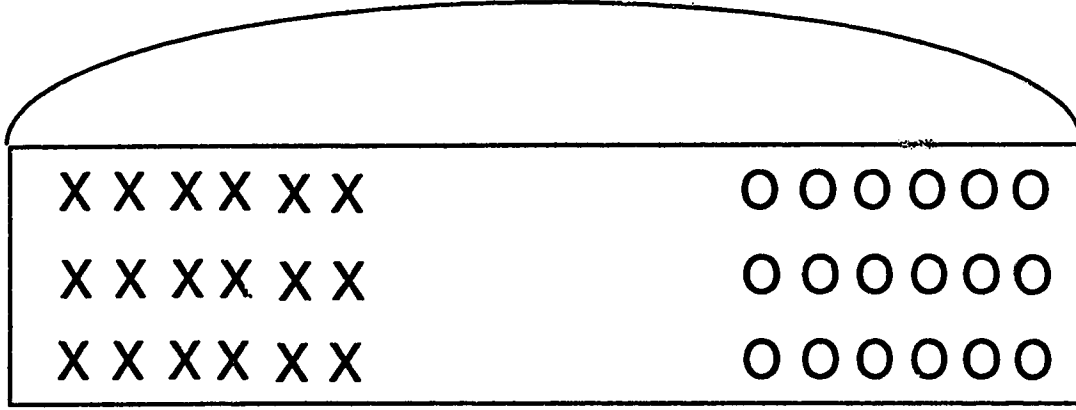


Figure 3.2: *Cross-section of a superconducting disk. The critical current distribution is considered as a series of concentric current loops.*

$$B_r(r, z) = \frac{\mu_0 I}{2\pi} \frac{z}{\{(r + r_i)^2 + z^2\}^{\frac{1}{2}}} \left[-K(k) + \frac{r^2 + r_i^2 + z^2}{(r - r_i)^2 + z^2} E(k) \right]. \quad (3.3)$$

Here K and E are complete elliptical integrals of the second kind, r_i is the radius of the i^{th} loop and I is the current flowing in this loop. The argument of the elliptical integrals is

$$k = \frac{4r_i r}{(r_i + r)^2 + z^2}. \quad (3.4)$$

The calculational procedure is as follows. Initially, a constant current density is set up within the sample. Using $I = J_c(r, z)\delta r\delta z$, where $\delta r\delta z$ is the cross sectional area of an individual current loop, and the above equations (3.2), (3.3) and (3.4), the local magnetic fields at each loop is calculated. The effective field affecting the critical current amplitude used in this paper is the magnitude of $|\vec{B}| = \sqrt{B_z^2 + B_r^2}$. As the critical currents are strongly dependent on the magnetic field, an iterative procedure is used and a new current distribution is calculated. The actual dependence of J_c on \vec{B} is discussed in sections 3.3 and 3.6. Further iterations are performed until a stable solution is achieved. This occurs satisfactorily within five iterations.

b) Extended Critical-State Model

In order to fully simulate shielding of the ceramic $\text{YBa}_2\text{Cu}_3\text{O}_{7-x}$ sample the standard critical state model as introduced by Bean had to be restructured. The magnetic shielding field profile above a ceramic superconductor is due to the superposition of the shielding fields produced by the intergrain transport currents and the intragranular surface currents. The calculation of the intragrain shielding was done with the model disk filled with non-interacting current loops simulating the currents, I_g , flowing on the surface of the superconducting grains. I_g were taken to be field independent. The current loops have the form of magnetic dipoles and generate the z and r components of the magnetic field at position (r, z) given by [45]:

$$\begin{aligned} B_z(r, z) &= \frac{3\mu_0 I_g a^2}{4} \frac{|r - x_i| z}{(|r - x_i|^2 + z^2)^{\frac{5}{2}}}, \\ B_r(r, z) &= \frac{\mu_0 I_g a^2}{4(|r - x_i|^2 + z^2)^{\frac{3}{2}}} \left(3 \frac{z^2}{(|r - x_i|^2 + z^2)} - 1 \right). \end{aligned} \quad (3.5)$$

Here, x_i is the position of the center of the current loop from the center of the disk. The quantity $I_g a^2$, where I_g is the loop current and a is the radius of the current loop, is not known exactly and has to be treated as a flexible parameter in the calculation. This parameter is denoted by ι . Calculations were made with a varied number of contributing intragranular loops placing them throughout the volume of the disk as well as only along the disk diameter. The results when considering current loops only along the disk diameter could be made equivalent to those from a large number of loops throughout the disk volume by increasing the value of ι . Thus to decrease computational time throughout this work, 160 diamagnetic loops along the disk diameter was taken and the various values of ι were used in the calculations of intragrain shielding. The typical values for ι will be discussed in a later section.

Flux flow at the disk edges discussed above destroys the superconducting shielding currents. Contributions of such effects can be simulated by removing the current, close to the sample edges, from the simulation in an attempt to include the

effects of flux motion.

3.6 Critical-State Model Simulation Constraints

a) Intergrain Critical Currents

There are several parameters dictating the numerical results of the critical-state simulation. Since the sample is considered to be filled with a series of concentric current loops in several planes, the effective width of each loop, δr , and the effective thickness of each loop, δz , will depend on the number of loops and the number of planes used in calculations. The size of the sample studied has an approximate radius of $8.0mm$. Thus, if the number of loops considered is N , the loop width becomes $\frac{8.0mm}{N}$. Likewise, the thickness of the sample was approximately $2.2mm$ and the effective loop width becomes $\frac{2.2mm}{N_{pl}}$, where N_{pl} is the number of planes used. Typical values used in calculations were $N = 80$, $\delta r = .01mm$, and $N_{pl} = 22$, $\delta z = .01mm$.

The magnetic field dependence of the critical current density is of major importance to the success of the critical state model. The discussion in section 3.3 lead to the averaging of equation 3.1 as a form for $J_c(\vec{B})$. The present work uses equation 3.1 as well as Kim's relation for $J_c(\vec{B})$ [32]. Kim's relation has the form

$$J_c(B) = \frac{\alpha}{(B + \beta)}.$$

There now exist four new parameters to be determined; α, β, B_0 and $J_c(0)$, for which a fit to experimental $J_c vs. B$ [35] data was done. The best fit was accomplished by utilizing equation 3.1 for magnetic fields below 30G and Kim's relation for fields above this point. Fig. 3.3 shows the results upon fitting the experimental data to the two forms of J_c . The parameters used have the following values.

- $\alpha = 1075.0$

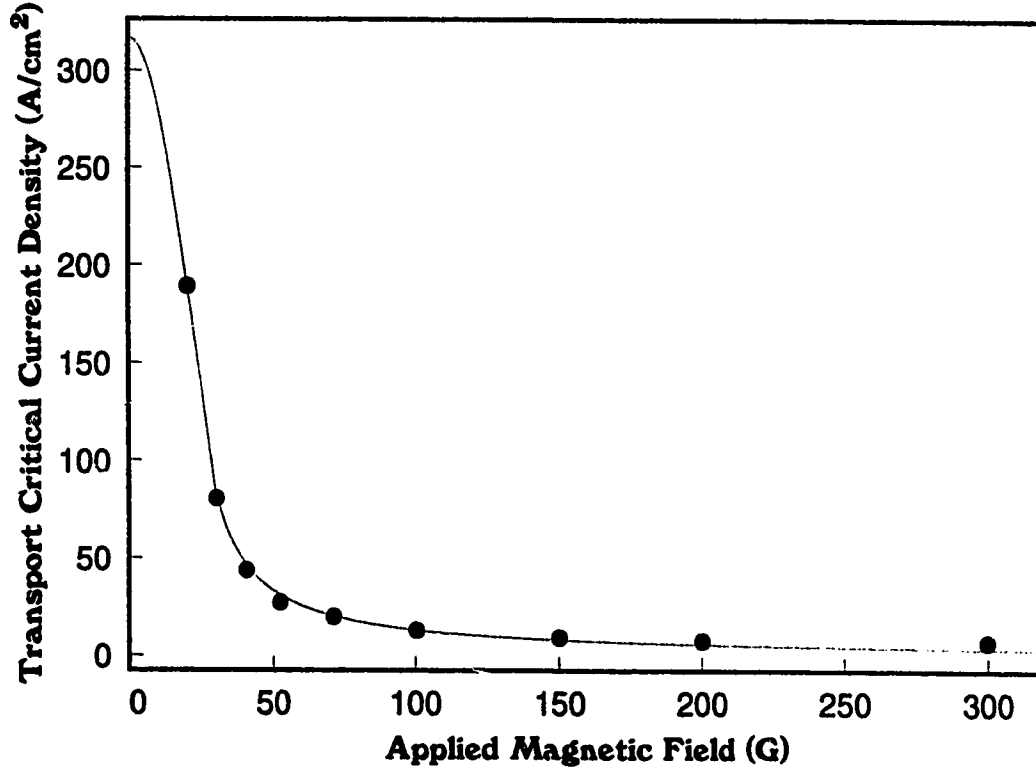


Figure 3.3: *Dependence of the transport critical current density on an applied field at 77K. Solid line shows fit used in simulation, circles are the experimentally obtained data [35].*

- $\beta = -17.5G$
- $B_0 = 38.7G$
- $J_c(0) = 317.0 \frac{A}{cm^2}$.

The critical current density distributions are determined both by the local magnetic fields and the areas of flux flow. At low applied magnetic fields shielding currents will not be induced in the interior of the sample. At higher fields, when flux begins to flow at the disk edges the currents will be dissipated. For computational purposes each plane has two parameters associated with it. These parameters dictate the width and location of current flow in that plane. With these distinctions, the

actual spatial distribution can be simulated by calculation.

b) Intragrain Shielding Field Simulation Constraints

As mentioned in section 3.5, the parameter ι will determine the contributions made by the intragranular current sources. As this parameter is completely arbitrary it serves as an indicator of the strength of the intragrain shielding capabilities. In fact, as will be discussed later on, the intragrain component of the shielding field comprises a large percentage of the total shielding field measured at the sample center.

3.7 Critical-State Model Simulation Results and Discussions

a) Full Critical State Shielding Field Profiles

Frankel compared the measured and calculated shielding field profiles of NbTi disks using the critical state model [33]. His results were duplicated and confirmed when his specific values for α and β in $J_c(B)$ were implemented in the simulation used in this paper. Däumling and Larbalestier extended Frankel's work to include disks of varying aspect ratios and the contribution of radial fields [34]. For instance, as found by Däumling and Larbalestier, for cases of field independent J_c (high applied fields), the axial shielding field profile is such that the field at the center of the disk is proportional to the sample thickness rather than its radius. At a distance $0.85 r_o$, r_o the sample radius, the axial field reverses polarity showing demagnetization effects. The shielding field at the center of the disk depends on the thickness of the sample rather than the radius. This result indicates the importance of sample geometry on the critical currents and magnetic properties of disk shaped samples.

The radial shielding field was also considered in this work. The radial field

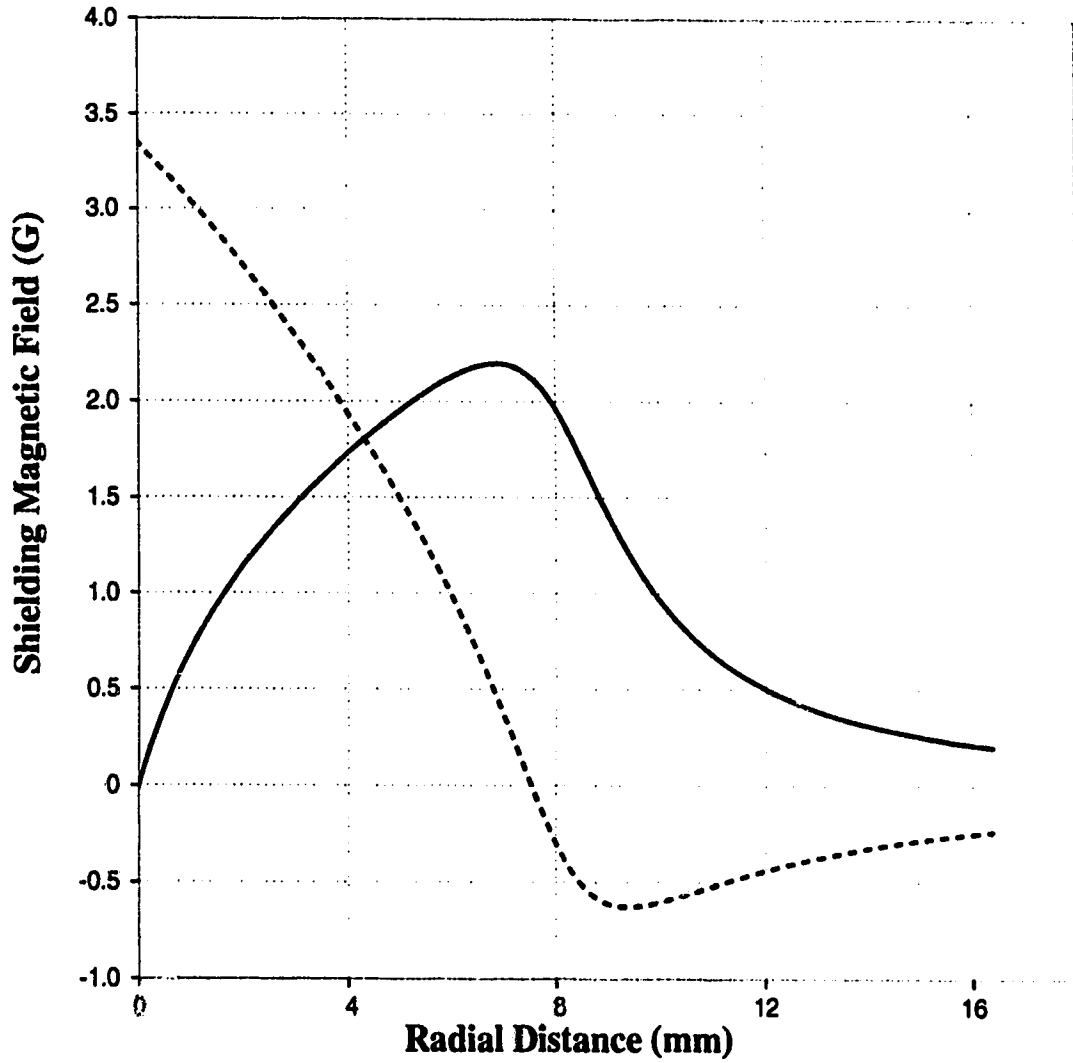


Figure 3.4: Axial (dashed) and radial (solid) shielding fields produced by intergrain currents only. The disk - shaped sample was in a full critical state and the currents were considered magnetic field dependent. The disk radius and thickness are 8 mm and 2.2 mm respectively.

distribution is such that it is zero along the sample axis ($r = 0$) and along the center plane ($z = 0$). Axially, the radial field is maximum on the sample surface and changes polarity as it crosses the center plane. This radial field is of significant magnitude and cannot be ignored when this model is applied to the disk shaped samples. In these samples, the radial field is as likely a contributor to the shielding currents as is the axial field.

Shown in Fig. 3.4 are the axial (dashed line) and radial (solid line) inter-granular shielding field profiles calculated in this work. The calculation was done considering a field dependent critical current and an aspect ratio of $r_o/d = 3.6$. The results are qualitatively the same as those described by Däumling and Larbalestier.

b) Intergrain Shielding Field Profiles

Following Bean's model, shielding currents will be induced in the areas of an existing flux gradient. For low applied magnetic fields, the axial flux gradient will be at the sample edge and fall to zero within a certain radial distance. The radial field however will exhibit a gradient through the sample surface [46] to a certain depth also inducing shielding currents to flow. The induced currents will flow within a certain spatial distribution dependent on the applied magnetic field.

If the sample is considered to be in a partial critical state, the spatial distribution of the current density may exist in many possible configurations. When the sample is exposed to increasing applied fields it is assumed that the currents arise in layered areas from the disk edges inward. Fig. 3.5 gives the contour plots of the current densities used to calculate the partial critical state shielding field profiles (Fig. 3.6). The profiles become sharper for large current removal meaning the gradients are larger than that of the full critical state sample.

The full critical state contour plot is given in Fig. 3.7(0.0 % of current removed)

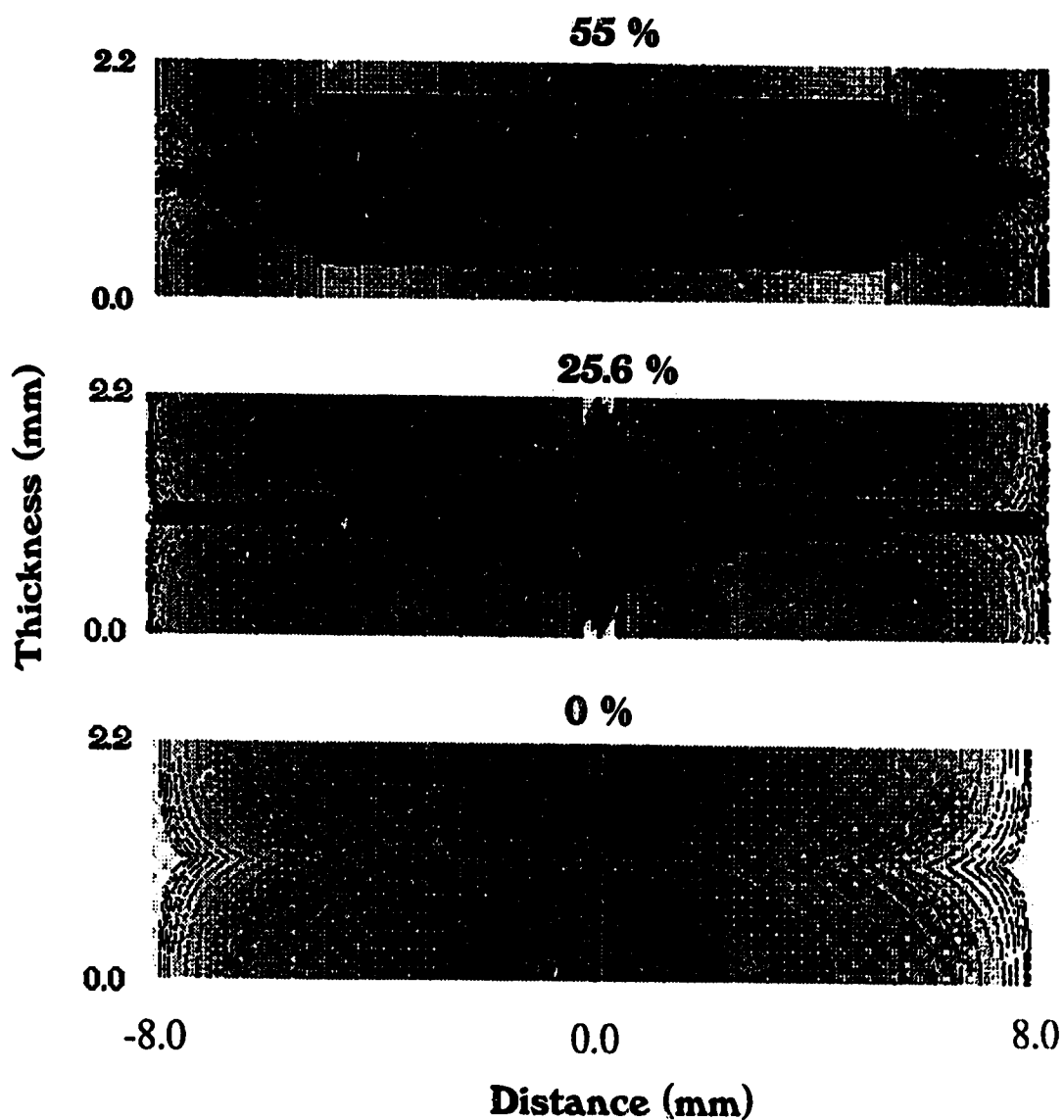


Figure 3.5: *Partial critical state current distribution. Black areas indicate zero current, white areas indicate maximum current. The contours are in steps of 20A. 55.0, 25.6 and 0.0% of the cross - sectional current area is removed.*

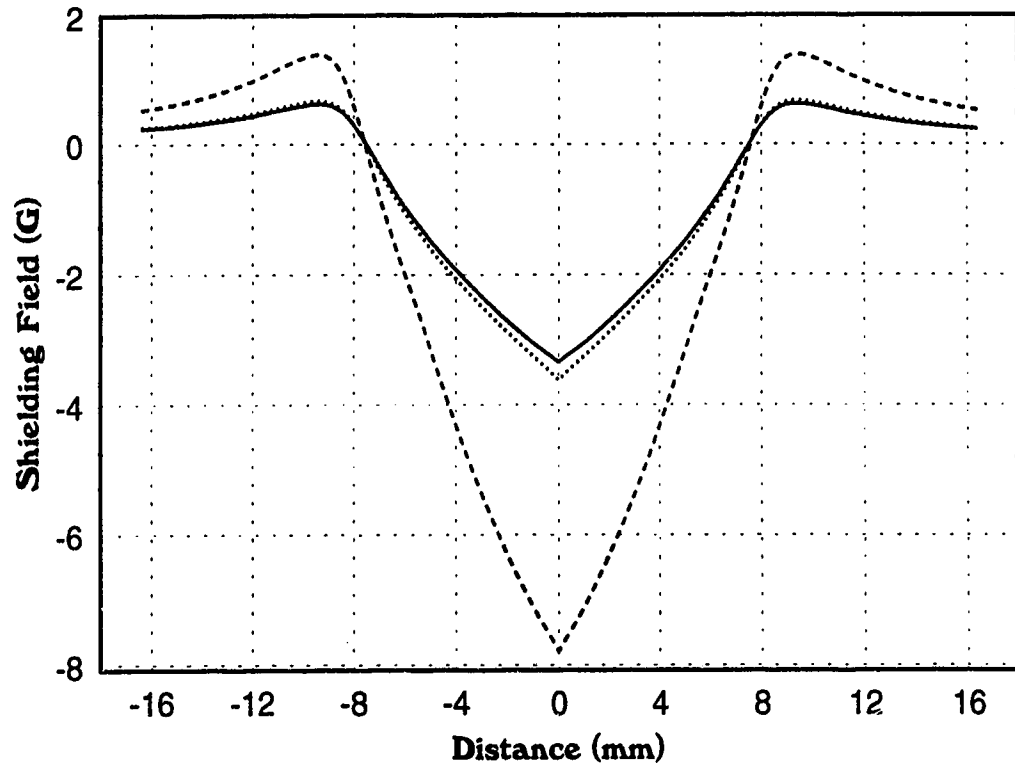


Figure 3.6: *Shielding fields produced by intergrain currents only. Solid line is the full critical state, dotted and dashed lines are profiles generated from partial critical state scenarios (25.6% and 55.0 % of the cross - sectional current area removed respectively).*

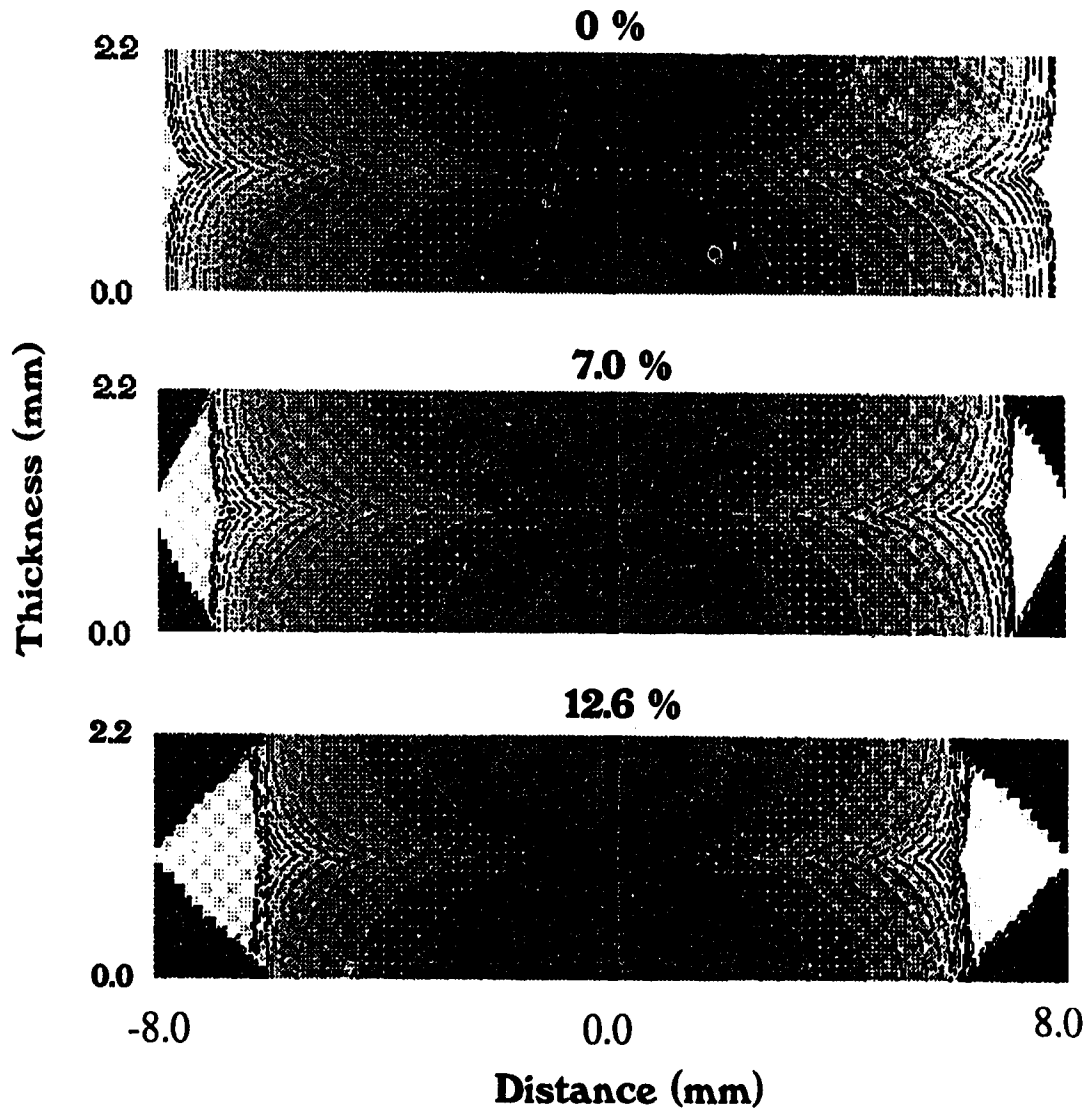


Figure 3.7: *Superconducting disk in a partial critical state current distribution. Here the currents near the disk edges are destroyed due to flux motion. Black areas indicate zero current, white areas indicate maximum current. The contours are in steps of 20A. 0.0, 7.0 and 12.6% of the cross - sectional current area is removed.*

and the profile is the solid line in Fig. 3.6. The demagnetization effects at the disk edges are more pronounced for the sample in the partial critical state. Simulations considering very thin layers of flowing current resulted in very sharp profiles with high demagnetization fields at the disk edges (dashed line). These profiles were not observed experimentally as the shielding field gradients are too large. The assumption is that the applied field necessary to produce a full critical state in the sample, H^* , is very low or close to H_{c1} such that a large fraction of the sample volume is always in the critical state.

The shielding field profile generated from a sample exposed to a field strong enough to produce flux flow at the edges is simulated by setting the currents at the edges of the sample to zero (Fig. 3.7).

The current distributions, given in Fig. 3.7, explicitly show the areas of zero current. Increasing the amount of flux flow (reducing the area of current flow) creates very sharp profiles with larger magnitudes at the center (Fig. 3.8). The profiles produced by considering extensive flux flow and current dissipation at the disk edge (see dashed line Fig. 3.8) were not observed experimentally as the shielding field gradients are too large. In fig. 3.8 the full critical state is shown as the dotted line. The solid line is generated from the distribution shown in Fig. 3.7 with 7% of the current removed.

c) Intragrain Shielding Field Profiles

Mohamed and Jung [35] showed that the magnitude of shielding field produced by pressed powder samples to be about 20 - 30% that of the ceramic superconductor. In the pressed powder sample, the only contributions to the shielding field are made by the currents flowing on the grain surfaces.

Calculated intragrain shielding fields are fit to the measured profiles of the

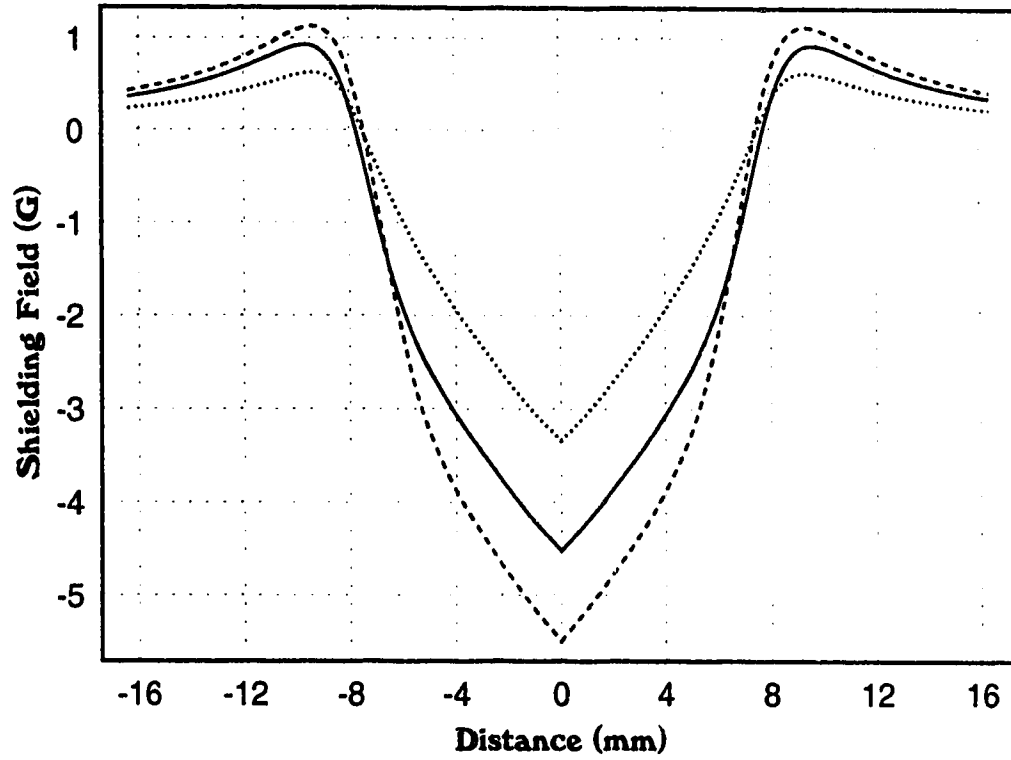


Figure 3.8: *Shielding field profiles generated from a full critical state (dotted line), and two partial states (solid line: 7% and dashed line: 13% of cross - sectional current area removed) resulting from flux flow dissipation of current (solid and dashed lines).*

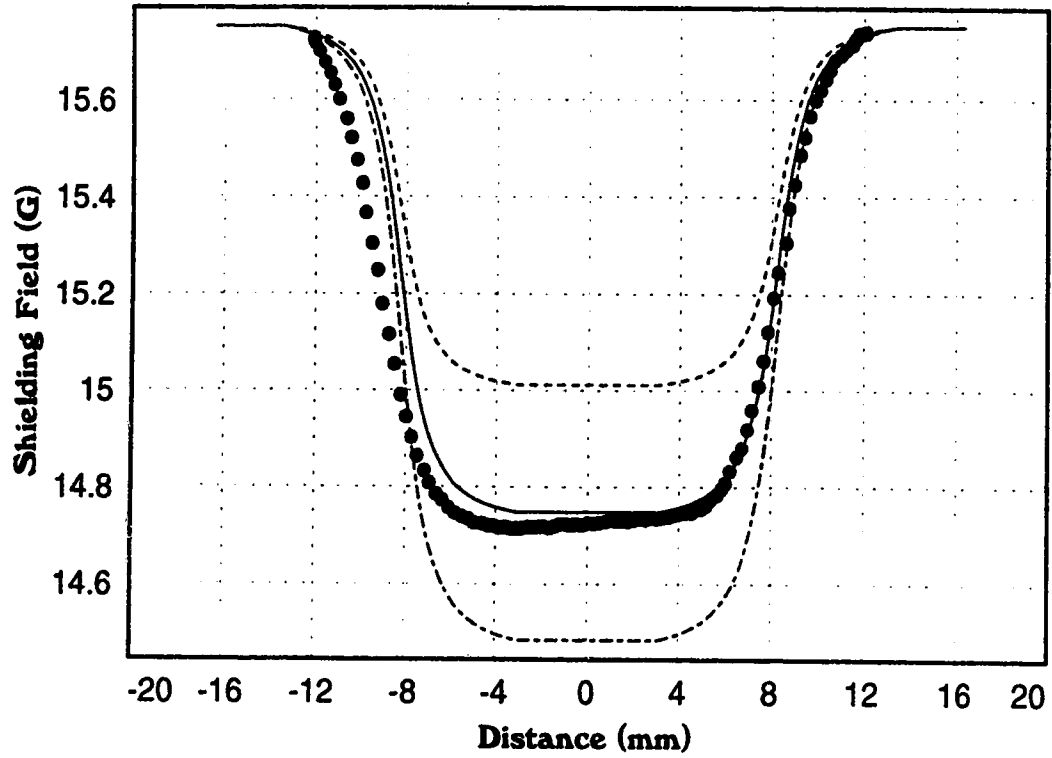


Figure 3.9: *Intragranular Shielding Fields. The measured data of Mohamed and Jung [35] of a pressed powdered sample in an applied field of 15 G. (black circles) is compared to the calculation of intragranular shielding fields alone. The parameter ι for the solid line is 30.4 Acm^2 , dotted line: 22.4 Acm^2 , and the dashed line: 38.4 Acm^2 .*

pressed powder sample. Fig. 3.9 shows the comparison of the intragrain shielding field calculations and the Hall probe data of a pressed powdered sample in 15 G.

The parameter used in analyzing the intragrain contributions is ι , (see section 3.5). Fig. 3.9 shows three different profiles calculated using three different values for ι . The best fit curve, the solid line, has $\iota = 30.4 \text{ Acm}^2$. The dotted line and dashed line have $\iota = 22.4 \text{ Acm}^2$ and $\iota = 38.4 \text{ Acm}^2$ respectively. Mohamed and Jung [35] stated that in higher applied fields, the transport currents within a $\text{YBa}_2\text{Cu}_3\text{O}_{7-x}$ ceramic superconductor are extinguished due to the decoupling of the grains. The shielding field profiles found in these scenarios are similar in shape to those measured for the

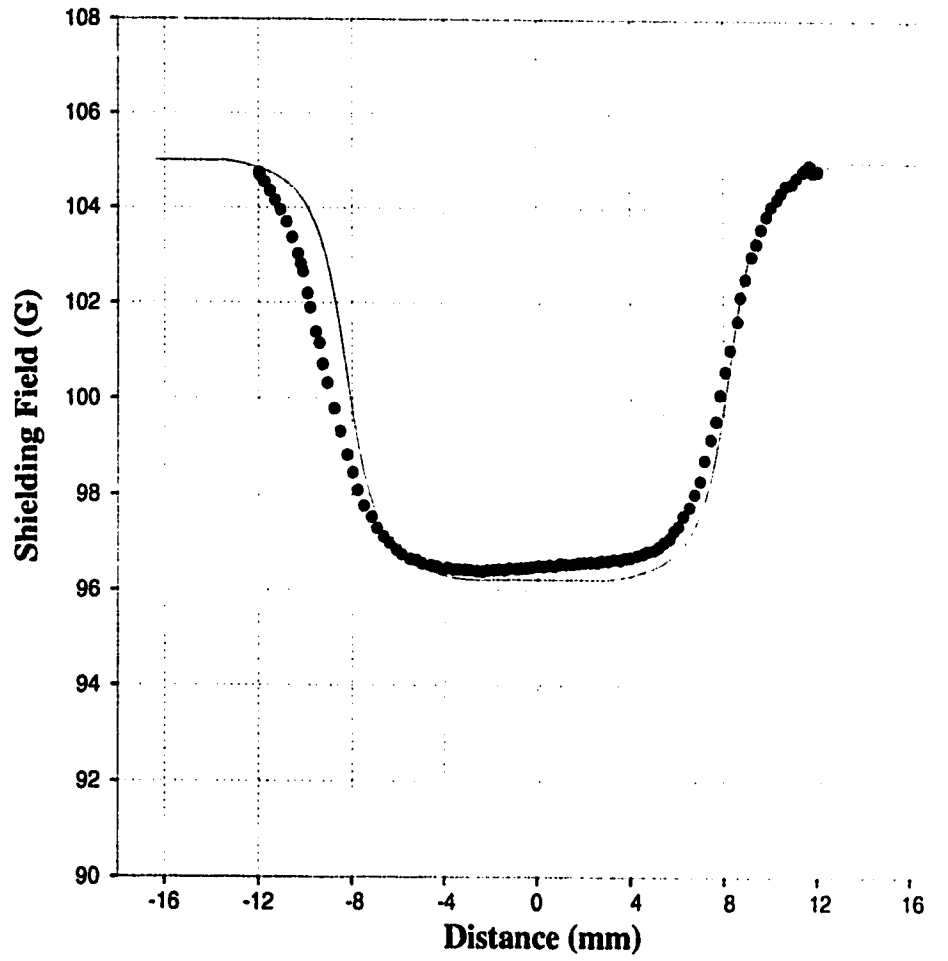


Figure 3.10: *The measured data of Mohamed and Jung [35] of a $YBa_2Cu_3O_{7-x}$ ceramic sample in an applied field of 100 G. (black circles) is compared to the calculation of intragranular shielding fields alone (solid line). The parameter ι is 2664 Acm^2 .*

pressed powder sample. A calculated profile utilizing only the intragrain shielding is used to fit the $\text{YBa}_2\text{Cu}_3\text{O}_{7-x}$ ceramic shielding field in an applied field of 100 G. (Fig. 3.10). The profile was generated using $\iota = 2664 \text{ Acm}^2$.

d) Ceramic Superconductor's Shielding Field Profiles

The shielding fields arising from ceramic samples is believed to originate from the superposition of intergrain and intragrain shielding fields and are modified by demagnetization effects. The data of Mohamed and Jung [35] taken of a ceramic $\text{YBa}_2\text{Cu}_3\text{O}_{7-x}$ sample in an applied field of 15 G is therefore compared to the calculated profile due to both intergrain and intragrain contributions (Fig. 3.11). The fit was achieved by taking the disk to be in a partial critical state (the distribution of Fig. 3.7, 7 % of current removed, was used) since flux flow at the disk edges was assumed to exist. A satisfactory fit was achieved by taking the intragranular contribution to comprise 50 - 60 % of the total shielding field at the center of the disk. This profile was calculated using $\iota = 200.4 \text{ cm}^2$, significantly higher than the values used to fit the data of the pressed powder sample in 15 G (see section c)). This indicates ceramic samples may have currents flowing over small clusters of grains which aid in more effectively shielding the sample than just the individual grains. Along with the transport currents these cluster currents would presumably also be destroyed during the pulverizing of the sample, and therefore not contribute in the shielding of the pressed powder sample.

e) Shielding Fields Dependent on Applied Field

In addition to studying the diamagnetic shielding field profiles measured across a superconducting ceramic disk, Mohamed and Jung [35] discussed the dependence of the shielding field on applied magnetic field. Their results show two maxima which

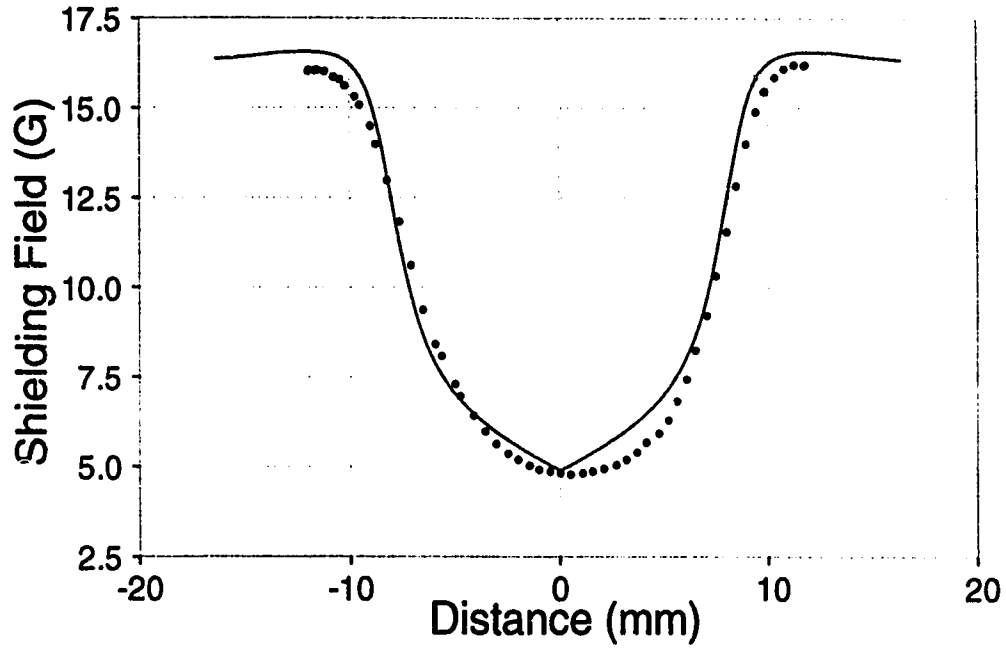


Figure 3.11: *Shielding field profile of ceramic sample. The measured data of Mohamed and Jung [35] of a ceramic $YBa_2Cu_3O_{7-x}$ sample in an applied field of 15 G. (black circles) is compared to the results of calculation made including both intergranular and intragranular diamagnetic shielding fields.*

they associate with the intergrain weak links. They measured the shielding field at various points along the disk's radius (Fig. 3.12). This picture gives an indication of the magnitude of the flux gradient and flux flow within the sample with varied applied field. For instance, the difference between the measured fields at each point along the disk's diameter is greatest at 25 - 35 G. The high gradients are catalysts for flux motion and their presence will in fact cause flux to flow and the dissipation in the shielding currents, causing the rapid drop in shielding fields noted at these applied fields.

This idea was scrutinized in the framework of the present work. The calculated shielding fields, due only to intergranular currents, at various distances on the diameter has been plotted, and in certain aspects reveal much the same characteristics as the measured data. Since the contribution of the applied field to the simulation can not be rigorously implemented, the altering of current distribution becomes the only method of addressing the issue. As previously discussed, a gradient of flux will, when strong enough, cause the motion of the flux and thus the dissipation of the critical currents. This gradient is shown in Fig. 3.11 to increase from the disk edges inward.

In the simulation a disk is taken in a full critical state, and the field is calculated at various points on the disk diameter (at the center, 2 mm, 4 mm, 6 mm, and 8 mm from the center). Then simulating the sample shielding in a higher applied field by reducing the amount of current flow at the disk edges the calculation is repeated. Figs. 3.13 - 3.15 give the current density plots used in the calculations. Fig. 3.16 gives the results.

Certain characteristics of the measured data are not reproducible. For instance, it is difficult to reproduce the changing contribution the intragranular shielding fields make as the applied field is increased. The reduction in shielding fields measured off the center is a result of the intergrain currents [35] and can be seen in Fig. 3.16.

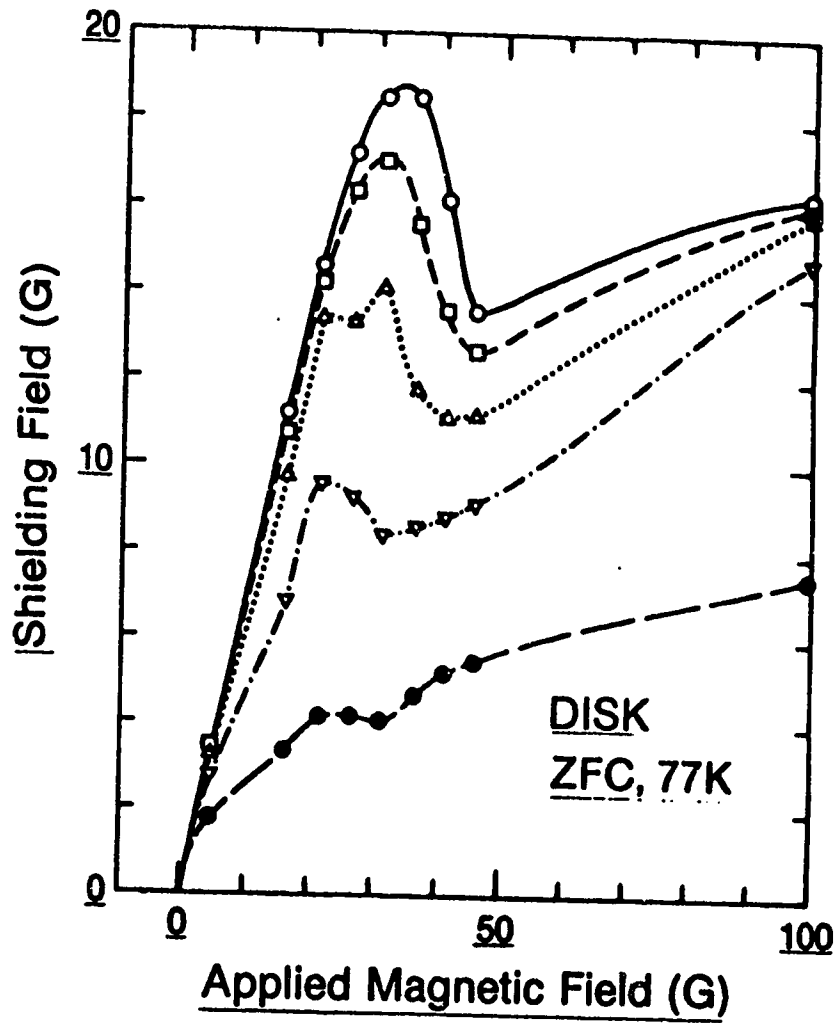


Figure 3.12: Dependence of the shielding field of ceramic $\text{YBa}_2\text{Cu}_3\text{O}_{7-x}$ on applied field. [35] Open circle: disk center, squares, triangles, inverted triangles and solid circles: points 2, 4, 6, 8 mm from center.

Note the gradients are much lower for fields of 40 G and higher suggesting the sample may be in a full critical state. However, Mohamed and Jung [35] point out that higher fields tend to decouple the grains and thus quench the superconducting intergrain currents leaving only the intragranular ones.

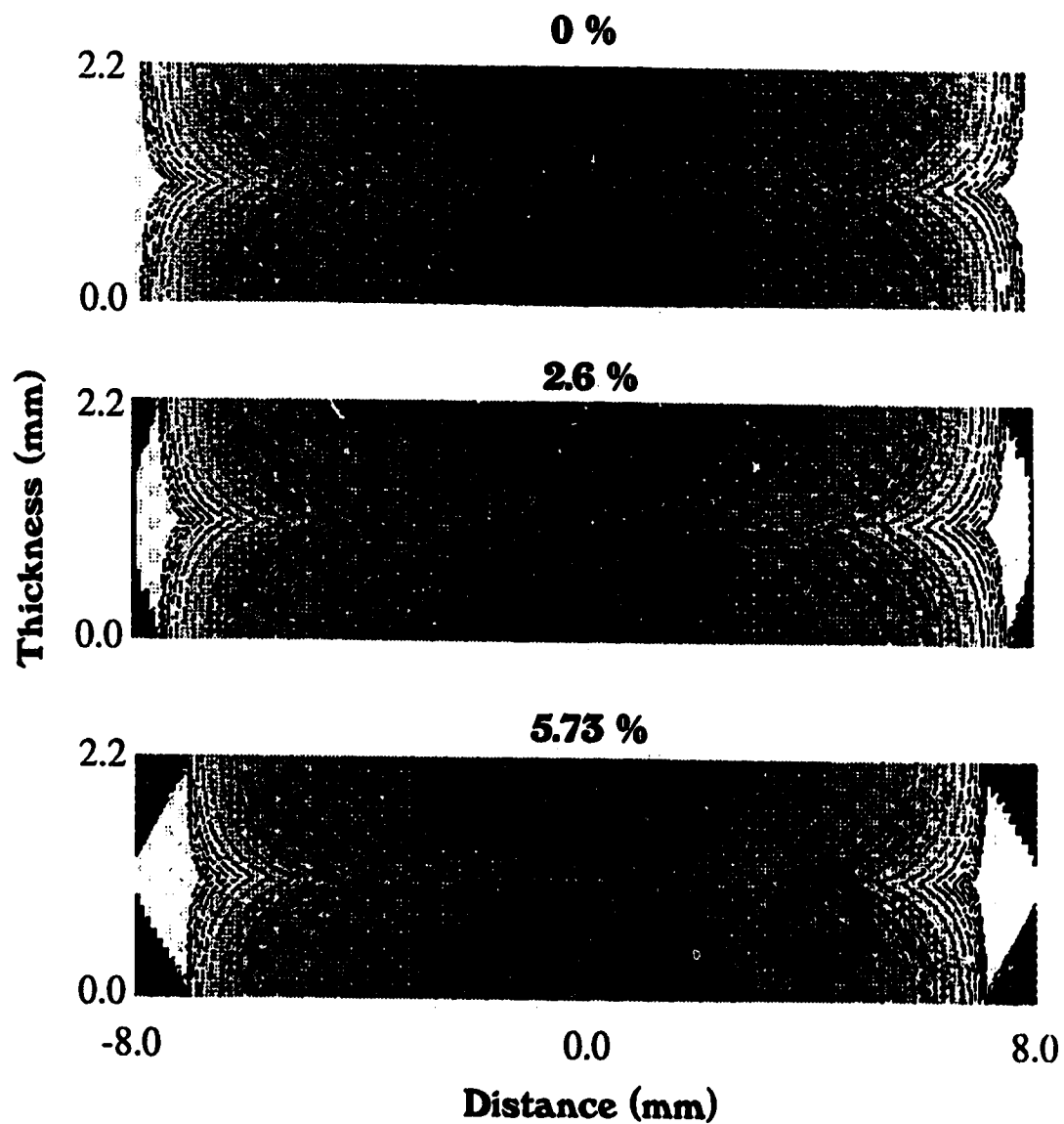


Figure 3.13: *Current distributions used in calculating the shielding field dependence on applied field. The distributions have 0, 2.6 and 5.73% of cross - sectional current area removed.*

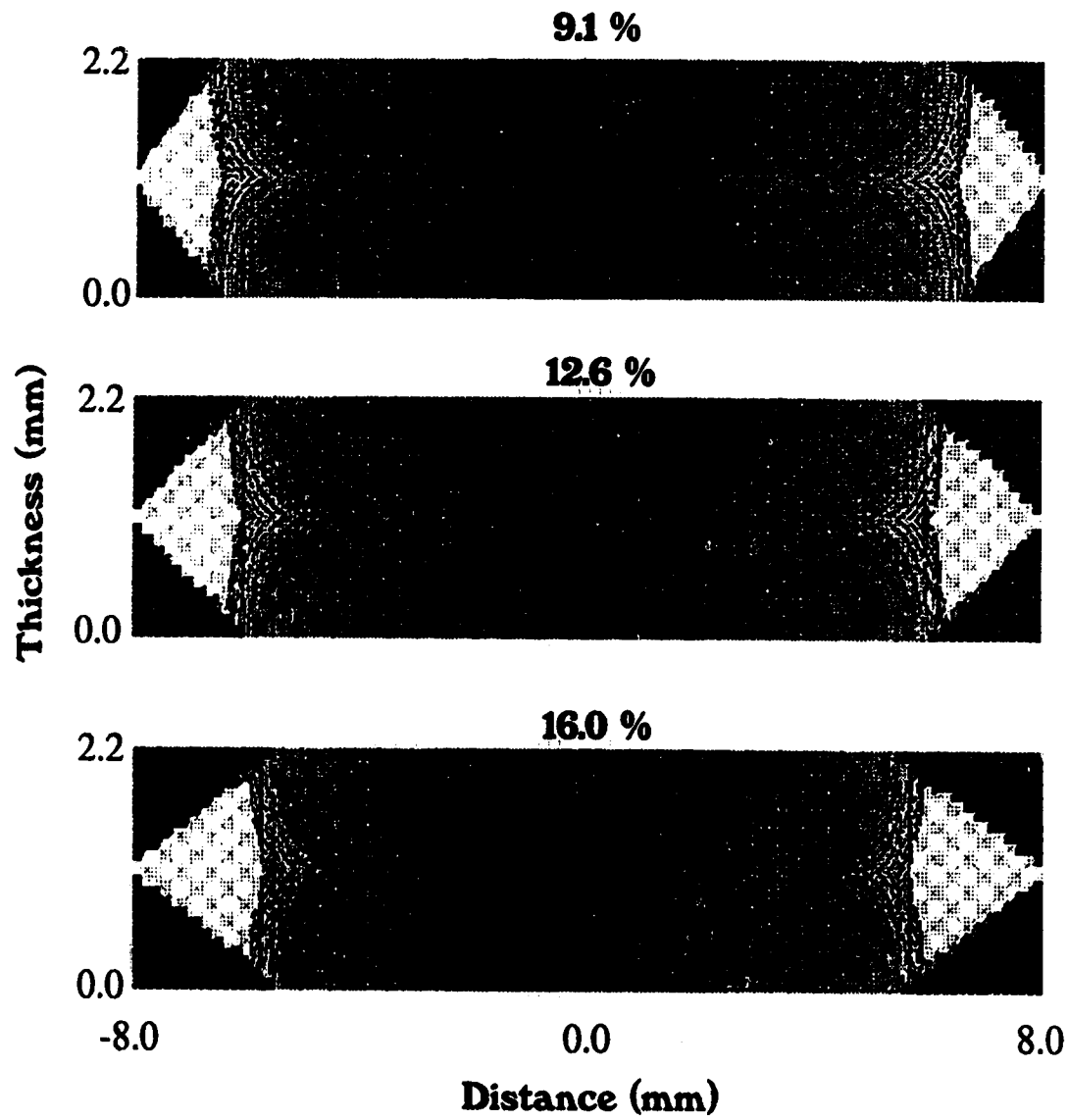


Figure 3.14: *Current distributions used in calculating the shielding field dependence on applied field. The distributions have 9.1, 12.6 and 16.0% of cross - sectional current area removed.*

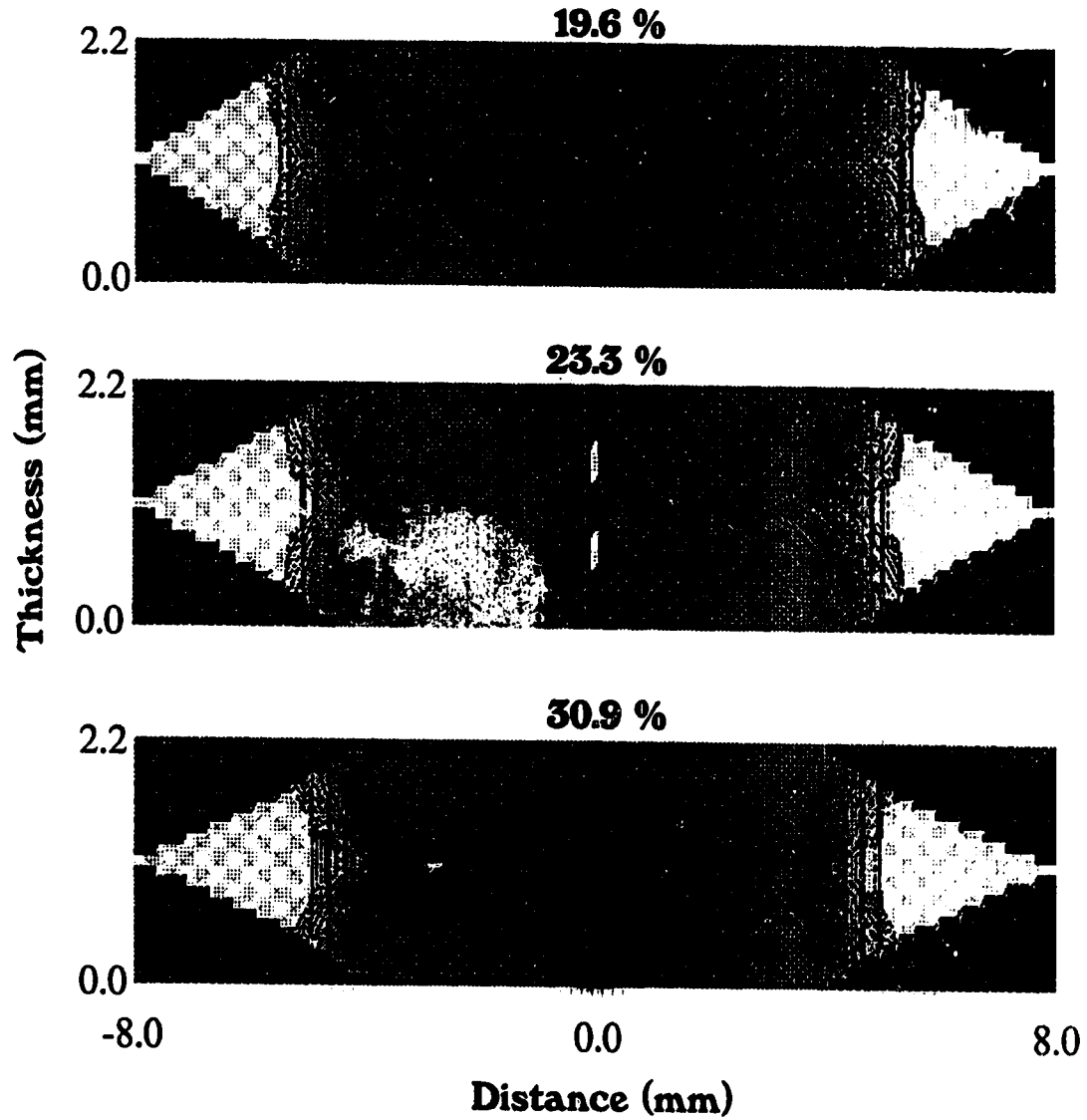


Figure 3.15: *Current distributions used in calculating the shielding field dependence on applied field. The distributions have 19.6, 23.3 and 30.9% of cross - sectional current area removed.*

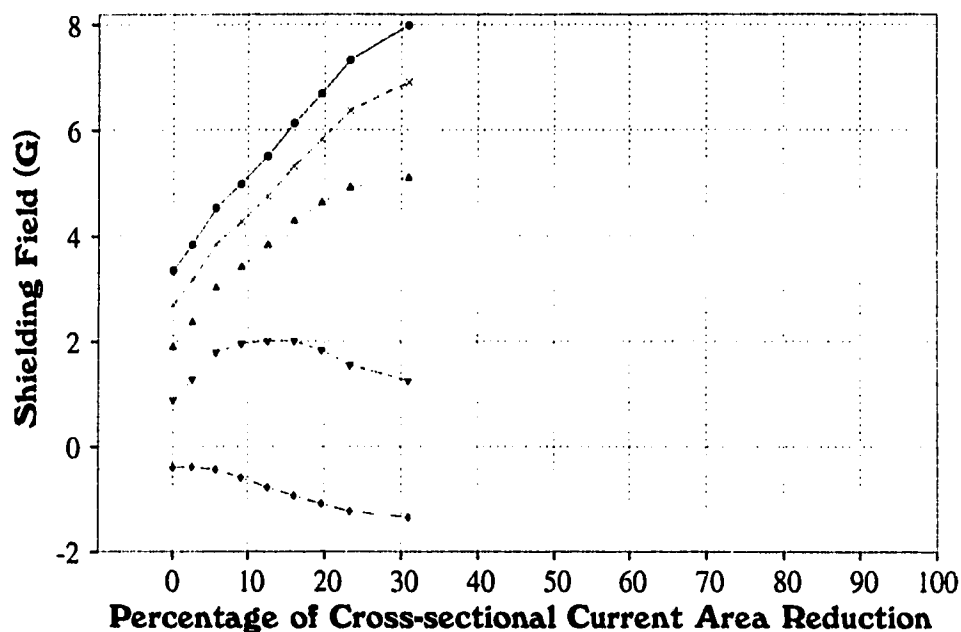


Figure 3.16: *Calculated shielding field dependent on current distribution (applied field). Each successive point on each curve was calculated using 0, 2.6, 5.73, 9.1, 12.6, 16.0, 19.6, 23.3, and 30.9% of cross - sectional current area removed. The curves (circles, x's, triangles, inverted triangles, and diamonds represent 0, 2, 4, 6, 8 mm from the disk center.*

CHAPTER FOUR

SUMMARY

This thesis investigated the magnetic and electrical properties of $\text{YBa}_2\text{Cu}_3\text{O}_{7-x}$ ceramics and $\text{YBa}_2\text{Cu}_3\text{O}_{7-x} + x\% \text{ Ag wt.}$ ceramic composites. The primary concern has been the role played by the intergrain weak links in the pinning and depinning of magnetic flux. Dc magnetization measurements were made on the samples. Two field cooling procedures were used, one with measurements made on slow cooling, the other with measurements made on warming after the sample was quickly cooled. These procedures allow for the observation of the intergrain flux depinning. An extended Bean model was used to study an $\text{YBa}_2\text{Cu}_3\text{O}_{7-x}$ ceramic's shielding processes. The intragrain currents, intergrain critical currents, flux flow, and demagnetization effects were all considered.

It was found that intergranular flux depinning occurs in ceramic $\text{YBa}_2\text{Cu}_3\text{O}_{7-x}$ samples. Adding silver to the compound alters the characteristics of the grain junctions thereby changing the depinning processes. The magnetization measurements of the different samples show the effect the addition of silver has on the intergranular depinning process. Sharp transitions from superconducting to normal states and narrow temperature ranges of active flux depinning indicate samples of high quality. The pure $\text{YBa}_2\text{Cu}_3\text{O}_{7-x}$ sample has a much sharper transition and the region of flux depinning exists in a smaller temperature interval than either the 2%wt. Ag doped $\text{YBa}_2\text{Cu}_3\text{O}_{7-x}$ sample or the 4%wt. Ag doped $\text{YBa}_2\text{Cu}_3\text{O}_{7-x}$ sample. Both of the silver doped samples have extended temperature ranges where flux is observed to be depinning. These samples have lower depinning energy and are less capable of preventing the inward motion of flux.

The temperature at which depinning of intergrain flux first occurs is the onset

temperature, T_o . This temperature is an indication of the energy needed to depin flux lines from their intergrain pinning sites. A phase diagram of H vs. T_o reveals the characteristics of each sample. It is observed that in applied fields up to 400 G, the addition of 2% Ag wt. reduces the necessary depinning energy from that needed for the pure $\text{YBa}_2\text{Cu}_3\text{O}_{7-x}$ sample. In fields below 125 G, the ceramic $\text{YBa}_2\text{Cu}_3\text{O}_{7-x}$ with 4% Ag wt. exhibits lower onset temperatures than that of the pure ceramic but higher onset temperatures than the $\text{YBa}_2\text{Cu}_3\text{O}_{7-x} + \text{Ag}$ (2% wt.) sample.

The completion temperature, T_d , denotes the temperature where the maximum rate of intergrain flux expulsion occurs. Above T_d penetration of flux into the sample becomes significant. The H vs. T_d phase diagram generally indicates $\text{YBa}_2\text{Cu}_3\text{O}_{7-x} + \text{Ag}$ (2% wt.) has its phase line shifted to lower temperatures than pure $\text{YBa}_2\text{Cu}_3\text{O}_{7-x}$ suggesting the silver doped sample cannot prevent the penetration of flux as well as the pure sample. On the other hand, in fields less than 50 Gauss, $\text{YBa}_2\text{Cu}_3\text{O}_{7-x} + \text{Ag}$ (4% wt.) effectively prevents flux penetration better than $\text{YBa}_2\text{Cu}_3\text{O}_{7-x} + \text{Ag}$ (2% wt.). For increased applied fields, 50 to 350 Gauss, the phase line in the H vs. T_d plane for $\text{YBa}_2\text{Cu}_3\text{O}_{7-x} + \text{Ag}$ (2% wt.) and $\text{YBa}_2\text{Cu}_3\text{O}_{7-x} + \text{Ag}$ (4% wt.) are similar.

The irreversibility line reveals the intragranular depinning processes. Upon comparison with the depinning of the intergrain flux, it is revealed that the intergrain depinning energy is less than for intragranular flux. The irreversibility line lies at significantly higher temperatures and fields than the phase lines of the ceramic samples.

Measurements of the depinning in very low fields, below 5 G., in pure $\text{YBa}_2\text{Cu}_3\text{O}_{7-x}$ revealed the maximum completion temperature achieved by the sample is 87.5 K. At higher temperatures the penetration of flux into the sample will always occur at a faster rate than the flux expulsion.

An extended Bean model was employed to develop an understanding of the magnetic properties of superconducting disk shaped ceramic samples. This simulation

takes its beginning from the work of Frankel and Däumling and Larbalestier [33, 34].

The present model is specifically geared toward simulating the shielding field profiles of the $\text{YBa}_2\text{Cu}_3\text{O}_{7-x}$ ceramic samples measured by Mohamed and Jung [35]. These samples exhibit different behaviour than the niobium base compounds studied by Frankel and Däumling and Larbalestier. These differences are the result of the sample's intrinsic characteristics, for example, its high anisotropy, granularity, and the intergrain flux behavior.

By changing the current distributions within the sample, the different stages of the evolution of the sample's shielding in an increasing applied field were reported. Intergrain shielding field profiles were generated for samples in various states. A sample is in a partial critical state when it is in an applied field low enough such that critical currents are not induced throughout the entire sample volume. The full critical state is achieved when the sample has transport currents flowing at the critical level throughout its volume. A second partial critical state was studied. This state exists as flux flows and critical currents are dissipated at the disk edges due to demagnetization effects.

Both the intergrain (transport) currents and the intragrain currents flowing on the surface of individual grains are contributing to the shielding of ceramic samples. This additional calculation of shielding field is done where the granular currents are assumed to be non-interacting current loops (dipoles). Shielding field profiles measured on pressed powdered samples are due to intragranular currents only; no intergrain transport currents exist. The results of the simulation give a good fit to the measured data obtained by Mohamed and Jung [35].

Shielding field profiles of disk - shaped ceramic samples were measured by Mohamed and Jung [35]. A simulation was made for the case in an applied field of 15 G by adding the shielding fields of both the intragranular currents and the intergrain transport currents. Flux motion at the disk corners was also assumed to exist. The

simulation results indicate that there may be further contributions to the shielding of a ceramic sample such as currents flowing on granular clusters rather than individual grains.

Mohamed and Jung [35] have measured shielding fields at various points along a ceramic disk's diameter as a function of magnetic field. Their results reveal the nature of the intergrain transport currents as determined by increasing applied field and sample geometry (demagnetization effects) An attempt to reproduce the shielding field characteristics due to the intergrain currents was done by eliminating the current flow in increasing amounts at the disk edges (simulating an increase in flux flow). Some general properties of the shielding field dependence on applied field could be reproduced by the computer computations.

BIBLIOGRAPHY

- [1] H. Kammerlingh Onnes, *Leiden Comm.* **120b**, **122b**, **124c** (1911)
- [2] M. Tinkham, *Introduction to Superconductivity* McGraw - Hill Book Co. New York (1975)
- [3] W. Meissner, R. Ochsenfel, *Naturwissenschaften* **21**, 787 (1933)
- [4] J. Bardeen, L. N. Cooper, J. R. Schrieffer, *Phys. Rev.* **108**, 1175 (1957)
- [5] V. L. Ginzburg, L. D. Landau, *Zh. Eksperim. i Teor. Fiz.* **20**, 1064 (1950)
- [6] A. A. Abrikosov, *Zh Eksperim. i Teor. Fiz* **32**, 1442 (1957) [*Soviet Phys. - JETP*, **5**, 1174 (1957)]
- [7] G. J. Dolan, G. V. Chardrashekar, T. R. Dinger, C. Feild, G. Holtzberg, *Phys. Rev. Lett.* **62**, 827 (1989)
- [8] J. G. Bednorz, K. A. Müller, *Z. Phys. B.* **64**, (1986) 189
- [9] A. Gupta, P. Esquinazi, H. Braun, and H. W. Neuüller, *Phys. Rev. Lett.* **63**, 1869 (1989)
- [10] Y. Yeshurun , A. P. Malozemoff, *Phys. Rev. Lett.* **60**, 2202 (1988)
- [11] M. Tinkham, *Phys. Rev. Lett.* **61**, 1658 (1988)
- [12] P. L. Gammel, L. F. Schneemeyer, J. V. Wasezak,, D. J. Bishop, *Phys. Rev. Lett.* **61**, 1666 (1988)
- [13] D. R. Nelson, *Phys. Rev. Lett.* **60**, 1973 (1988)
- [14] E. H. Brandt, *Phys. Rev. Lett.* **63**, 1106 (1989)

- [15] A. Houghton, R. A. Pelcovits, S. Sudo, *Phys. Rev. B* **40**, 6763 (1989)
- [16] R. Schmucker, E. H. Brandt, *Phys. Stat. Sol.* **79**, 479 (1977)
- [17] S. Koka, K. N. Shrivastava, *Sol. State Comm.* **75**, 911 (1990)
- [18] M. V. Feigel'man, V. M. Vinokur, *Phys. Rev. B* **41**, 8986 (1990)
- [19] G. Eilenberger, *Phys. Rev.* **164**, 628 (1967)
- [20] M. A. Moore, *Phys. Rev. B* **39**, 136 (1989)
- [21] K. N. Shrivastava, *Phys. Rev. B* **41**, 11168 (1990)
- [22] K. A. Müller, M. Takashige, J. G. Bednorz, *Phys. Rev. Lett.* **58**, 1143 1987
- [23] R. Labusch, *Phys. Stat. Sol.* **32**, 439 (1969)
- [24] M. P. A. Fisher, *Phys. Rev. Lett.* **63**, 1106 (1989)
- [25] Youwen Xu, M. Suenaga, *Phys. Rev. B* **43**, 5516 (1991)
- [26] T. T. M. Palstra, B. Batlogg, R. B. Van Dover, L. F. Schneemeyer, J. V. Waszczak, *Phys. Rev. B* **41**, 6621 (1990)
- [27] T. T. M. Palstra, B. Batlogg, R. B. Van Dover, L. F. Schneemeyer, J. V. Waszczak, *Appl. Phys. Lett.* **54**, 763 (1989)
- [28] J. Jung, M. A.-K. Mohamed, *Journal of Advanced Science (Japan)* **4**, 50 (1992)
- [29] A. Mumtaz, H. Athar, S. K. Hasanain, Jamil A. Khan, *Solid State Communi.* **79**, 601 (1991)
- [30] D. X. Chen, R. C. Goldbarb, J. Nogues, K. V. Rao, *J. Appl. Phys.* **63**, 980 (1990)
- [31] C. P. Bean, *Rev. Mod. Phys.* **36**, 31 (1964)
- [32] Y. B. Kim, C. F. Hempstead, A. R. Strnad, *Phys. Rev* **129**, 528 (1963)

- [33] D. J. Frankel, *J. Appl. Phys.* **50**, 5402 (1979)
- [34] M. Däumling, D. C. Larbalestier, *Phys. Rev. B*, **40**, 13, 9350 (1989)
- [35] M. A.-K Mohamed, J. Jung, *Phys. Rev. B*, **44**, 9, 4512 (1991)
- [36] H. Dersch, G. Blatter, *Phys. Rev. B* **38**, 11391 (1988)
- [37] S. Shimamoto, *Cryogenics* **14**, 641 (1974)
- [38] M. K. Wu, J. R. Ashburn, C. J. Torng, P. H. Hor, R. L. Meng, L. Gao, Z. J. Huang, Y. Q. Wang, C. W. Chu, *Phys. Rev. Lett.* **58**, 908 (1987)
- [39] H. K  pfer, I. Apfelstedt, W. Schauer, R. Flukiger, R. Meier-Hirmer, H. Wuhl, *Z. Phys. B* **69**, 159 (1987)
- [40] D.P. Hampshire, X. Cai, J. Seuntjens, D. C. Larbalestier, *Superconductor Sci. Technol.* **1**, 12 (1988)
- [41] T. Van Duzer and C. W. Turner, *Principles of Superconductive Devices and Circuits*(Elsevier, New York, 1981), Chap. 4
- [42] R. L. Peterson, J. W. Ekin, *Phys. Rev. B* **37**, 9848 (1987)
- [43] M. A-K. Mohamed, J. Jung, J. P. Franck, *Phys. Rev. B* **39**, 9614 (1989)
- [44] W. R. Smythe, *Static and Dynamic Electricity* (McGraw-Hill, New York, 1939), p. 266.
- [45] Jackson, J. D. *Classical Electrodynamics* John Wiley and Sons Inc. New York (1975) 182-183.
- [46] L. W. Conner, A. P. Malozemoff, *Phys. Rev. B* **43**, 402 (1991)